METAL-POOR DWARF GALAXIES IN THE SIGRID GALAXY SAMPLE. I. H II REGION OBSERVATIONS AND CHEMICAL ABUNDANCES

David C. Nicholls[1], Michael A. Dopita[1,2], Ralph S. Sutherland[1], Helmut Jerjen[1],
Lisa J. Kewley[1], and Hassan Basurah[2]

[1] Research School of Astronomy and Astrophysics, Australian National University, Cotter Road, Weston ACT 2611, Australia; David.Nicholls@anu.edu.au
[2] Astronomy Department, King Abdulaziz University, P.O. Box 80203 Jeddah, Saudi Arabia

ABSTRACT

In this paper we present the results of observations of 17 H II regions in thirteen galaxies from the SIGRID sample of isolated gas-rich irregular dwarf galaxies. The spectra of all but one of the galaxies exhibit the auroral [O III] 4363 Å line, from which we calculate the electron temperature, T_e, and gas-phase oxygen abundance. Five of the objects are blue compact dwarf galaxies, of which four have not previously been analyzed spectroscopically. We include one unusual galaxy which exhibits no evidence of the [N II] $\lambda\lambda$ 6548,6584 Å lines, suggesting a particularly low metallicity ($< Z_\odot/30$). We compare the electron temperature based abundances with those derived using eight of the new strong-line diagnostics presented by Dopita et al. Using a method derived from first principles for calculating total oxygen abundance, we show that the discrepancy between the T_e-based and strong-line gas-phase abundances have now been reduced to within $\sim$0.07 dex. The chemical abundances are consistent with what is expected from the luminosity–metallicity relation. We derive estimates of the electron densities and find them to be between $\sim$5 and $\sim$100 cm^{-3}. We find no evidence for a nitrogen plateau for objects in this sample with metallicities $0.5 > Z_\odot > 0.15$.

Key words: galaxies: dwarf – galaxies: evolution – galaxies: formation – galaxies: irregular – H II regions – ISM: abundances

Online-only material: color figures

1. INTRODUCTION

The metallicity of H II regions in small isolated dwarf galaxies is key to investigating the physical processes that govern star formation in undisturbed stellar systems.[3] The Small Isolated Gas Rich Irregular Dwarf galaxy (SIGRID) sample of small isolated gas-rich irregular dwarf galaxies (Nicholls et al. 2011) was selected with the aim of exploring the behavior of the mass– or luminosity–metallicity relation at the low end of the mass scale. This is based on the observation that nebular metallicity decreases with galaxy stellar mass/luminosity (see, for example, Tremonti et al. 2004; Lee et al. 2006). However, the low end of the mass scale shows significantly more scatter in metallicity than the high end in the Tremonti Sloan Digital Sky Survey (SDSS) data. By selecting isolated dwarf galaxies, it was our intention to see if this scatter persisted, and whether it was an intrinsic property of small galaxies. The SIGRID study is complementary to the "Choirs" study which looks for tidal dwarf emission line galaxies in group environments (Sweet et al. 2014). It is distinct from the Spitzer Local Volume Legacy survey used by Berg et al. (2012) and the SDSS data of Tremonti et al. (2004) in using targets specifically chosen for their isolation. It is most similar in concept to the study by Pustilnik et al. (2011) of galaxies in the Lynx-Cancer void, but is limited to small very isolated dwarf objects.

Other questions that the SIGRID observations are intended to address are the existence or otherwise of a primary nitrogen "plateau" at metallicities below $Z = 8.45$ (van Zee et al. 1998a),

and the relationship between oxygen abundances determined using "direct method," based on the measurement of the electron temperature and the estimation of the ionization correction factors to account for unseen ionization stages, and "strong-line" technique, based on a calibration of the bright emission lines and emission line ratios.

There has not been good agreement to date between the two methods, attributed to the empirical nature of the strong-line methods. They have been calibrated in terms of the direct method, and have not until recently had an analytical basis. The direct method has been used as a standard for temperature and metallicity measurement, against which the strong-line methods have been calibrated. Dopita et al. (2013) subsequently presented a set of strong-line diagnostic grids derived from the Mappings photoionization modeling code, based on the latest atomic data (see Nicholls et al. 2013). We use both the new atomic data and the new diagnostic grids in our analysis.

One might expect there to be greater scatter in the mass–metallicity relation at low masses, due to (1) measurement noise in nebular spectra in fainter galaxies, and (2) different star formation histories in the galaxies. Lee et al. (2006) suggest that the apparent scatter diminishes in observations at longer wavelengths (4.5 μm), and we present additional optical spectral evidence on this question.

The behavior of the ratio of nitrogen to oxygen abundances at low metallicities also shows increased scatter at lower metallicity. The current consensus appears to be that there is a low metallicity plateau in log(N/O), indicating the existence of primary nitrogen (see, for example, Vila Costas & Edmunds 1993; van Zee et al. 1998a; Contini et al. 2002; van Zee & Haynes 2006; Pilyugin et al. 2010; Pérez-Montero & Contini 2009; Berg et al. 2012; Andrews & Martini 2013). However, these previous works were not confined to small isolated dwarf

---

[3] In this paper we attempt to be explicit in our terminology, using the term "oxygen abundance," and referring to "metallicity" only in widely used terms such as "mass–metallicity" and to refer to total chemical abundances. In addition, the abundance of oxygen measured from spectra is the gas-phase abundance, and does not take into account the oxygen in dust grains.

Table 1
Observations of Objects from SIGRID Sample

Object (HIPASS ID)	Alternate ID (NED)	R.A. (J2000)	Decl. (J2000)	Observed (date)	Exp. (minute)	Seeing (arcsec)	Aur. (#)	D (Mpc)	$\log(m_{\rm H\,I})$ ($m_{H_{\odot}}$)	M_R (mag.)	Delta Index	Comments
J0005−28	ESO149-G013	00 05 31.8	−28 05 53	2011 Aug 27	60	1.5	1	10.2	8.23	−15.3	−2.1	BCD
J1118−17(s2)	n/a	11 18 03.1	−17 38 31	2011 Mar 13	80	1.5	0	13.5	8.56	−13.5	−2.2	v. low N II
J1152−02A,B	UGC 06850	11 52 37.2	−02 28 10	2011 Mar 7	60	2.2	2	13.5	8.31	−16.7	−1.7	BCD
J1225−06s2	LEDA 1031551	12 25 40.0	−06 33 07	2010 May 11	60	2.8	1	20.2	8.48	−14.2	−1.5	
J1328+02	LEDA 135827	13 28 12.1	+02 16 46	2010 May 13	40	1.8	1	15.5	7.93	−15.2	−0.7	
J1403−27	ESO510-IG052	14 03 34.6	−27 16 47	2010 May 11	60	3–5	1	17.5	8.72	−16.6	−1.8	BCD
J1609−04[2][5]	MCG-01-41-006	16 09 36.8	−04 37 13	2011 Aug 25	60	2–2.4	2	14.8	8.30	−16.1	−2.9	
J2039−63A,B	LEDA 329372	20 38 57.2	−63 46 16	2009 Sep 16	60	1.3	2	22.8	8.31	−16.5	−1.4	BCD
J2234−04B	MCG-01-57-015	22 34 54.7	−04 42 04	2011 Aug 26	60	1.3	1	20.5	8.50	−16.2	−0.2	
J2242−06	LEDA 102806	22 42 23.5	−06 50 10	2010 Jul 9	60	1.8–2	1	14.1	7.95	−15.6	−0.7	
J2254−26	MCG-05-54-004	22 54 45.2	−26 53 25	2009 Sep 16	60	1.3	1	12.1	8.46	−16.1	−2.1	BCD
J2311−42A,B	ESO291-G003	23 11 10.9	−42 50 51	2011 Aug 27	60	1.8–2	2	19.1	8.19	−16.5	−1.3	
J2349−22	ESO348-G009	23 49 23.5	−22 32 56	2010 Oct 6	80	1.8–2	1	7.7	7.99	−14.7	−0.5	

Notes.
[a] Object data from Nicholls et al. (2011).
[b] Columns 1 and 2: object ID; Columns 3 and 4: coordinates; Column 5: observation date; Column 6: exposure time on object; Column 7: regions with [O III] auroral line; Column 8: distance (Mpc); Column 9: neutral hydrogen mass; Column 10: R-band-magnitude; Column 11: isolation index; Column 12: comments.

galaxies. Results in our earlier paper on two isolated Local Void dwarf galaxies (Nicholls et al. 2014), indicated that log(N/O) did not plateau at low metallicity, suggesting no evidence for primary nitrogen. In this paper we present additional evidence for this.

The paper is structured as follows: in Section 2 we detail the sample selection, the spectroscopic observations, and the data reduction details. Hα images of each observed target, spectra, and de-reddened nebular emission line fluxes are presented in Section 3. In Section 4 we present the principal results of the analyses: electron temperatures, gas-phase nebular metallicities with the diagnostic grids, the nitrogen to oxygen flux ratios, the [S II] line ratios and electron densities, and the luminosity–metallicity results. In Section 5 we discuss these results, including the anomalies, and in Section 6 we present our conclusions. A discussion of methods used to estimate errors in the emission line fluxes is given in the Appendix.

2. OBSERVATIONS

2.1. Sample Selection

The SIGRID sample was selected to identify small isolated gas-rich irregular dwarf galaxies using the criteria described in Nicholls et al. (2011). All objects are members of the Survey for Ionization in Neutral Gas Galaxies (SINGG) catalog (Meurer et al. 2006), selected from their H I signatures in the H I Parkes All-Sky Survey (HIPASS; Meyer et al. 2004) and the presence of Hα emission from star-forming regions. From this sample we have, to date, observed 34 objects using Integral Field Unit (IFU) optical spectroscopy, as detailed below. From these observations we report here on 12 galaxies where the [O III] auroral line is evident, allowing us to calculate the electron temperature T_e, and the gas-phase oxygen abundance; and an additional galaxy, J1118−17, with an unusual spectrum with no observed [N II] lines. In four objects, two separate H II regions were observed which exhibited the auroral line, resulting in 18 separate H II region observations. Three objects (J1152−02, J1225−06, J1328+02) are not members of the final SIGRID sample, but had been observed during the refining of that sample. They were later excluded due to possible influence by regional galaxy groups and clusters, although they are clearly isolated

objects, as evidenced by their isolation Δ index values (Nicholls et al. 2011). Five objects qualify as blue compact dwarf (BCD) galaxies, using the definition by Sung et al. (2002) and discussed by Nicholls et al. (2011), though they have not previously been identified as such.

2.2. Spectroscopic Observations

The targets were observed using the WiFeS IFU spectrograph (Dopita et al. 2007, 2010) on the Australian National University 2.3 m telescope at Siding Spring. The WiFeS instrument is a double-beam image-slicing IFS, designed specifically to maximize throughput. It covers the spectral range 3500–9000 Å, at resolutions of 3000 (full spectral range) and 7000 (long wavelength limit 7000 Å). It has a science field of view (FOV) of 25 × 38 arcsec. As most of the SIGRID objects subtend angles less than its FOV, WiFeS is an ideal instrument to measure nebular metallicities in the ionized hydrogen star-forming regions. The instrument generates a data cube that allows exploration of nebular and continuum spectra in different regions of the target objects. Typically, even in poor seeing WiFeS resolves SIGRID object star formation regions easily, making possible exploration of excitation and abundances in different regions of each object. In these observations, resolutions used were $R = 3000$ for the blue camera and $R = 7000$ for the red, spanning a usable wavelength range of ∼3600–7000 Å. Short period (150 s on object, 75 s on sky) nod-and-shuffle observations were used for all objects, to allow near-complete removal of the sky lines. The exposure times recorded in Column 5 of Table 1 are the on-object integration times.

Details of the observations are given in Table 1. The sample is described in detail in Nicholls et al. (2011): essentially, the objects lie between redshifts of 300 and 1650 km s^{-1}, have neutral hydrogen masses less than and R-band magnitudes fainter than the Small Magellanic Cloud, low rotation velocities, show evidence of current active star formation, and are isolated, away from galaxy clusters and the tidal effects of other galaxies. All objects exhibit low (gas-phase) oxygen abundance (log(O/H) $\lesssim Z_{0.3\odot}$), as we describe below. The seeing listed in Column 7 shows that in all but one case, (J1403−27), the

seeing was average for Siding Spring. Even in that case, the seeing was better than the spaxel sample size, resulting in little if any flux loss.

Several classes of object were identified in Nicholls et al. (2011), including "bloaters," which are objects considerably more spatially extended than their masses would suggest. One of these is J1118−17. It is very faint, but as we show below, appears to have a very low metallicity. In the light of the results obtained for the relatively faint object, J1118−17 (s1 and s2 targets), it would have been desirable to undertake significantly longer integration times, but observing conditions (weather and moonlight) did not permit this. We intend to undertake further longer integration time observations for this unusual object. The spectrum of J1118−17s1 is very noisy with few usable spectral lines, so we have analyzed only s2—the two objects appear similar apart from luminosity. We reported results for J1609−04, a very isolated galaxy at the edge of the Local Void, in a previous paper (Nicholls et al. 2014), and the results are included again here for completeness.

2.3. Data Reduction

The data were reduced using the revised WiFeS Python "Pywifes" pipeline (Childress et al. 2013). This involves steps generally similar to those described in Dopita et al. (2010) for the older pipeline: bias modeling and subtraction, flat fielding, arc line identification and wavelength calibration, cosmic ray removal, sky-line subtraction using nod-and-shuffle, initial data cube construction and atmospheric dispersion correction, standard flux star calibration, telluric correction, assembly into the final data cubes and, where necessary, combination of multiple cubes into a final object data cube. The standard stars used were taken from Bessell (1999). Spectral sampling was undertaken using a 6 arcsec diameter circular spatial area centered on each H II region, through the full wavelength range of the data cube, to obtain spectra for each region. Line fluxes were measured from these spectra using IRAF/splot. Particular care was taken to account for any stellar absorption features underlying the Balmer emission lines, although in all cases, this was minor or absent, due to low stellar continuum. In fact, the stellar continuum was extremely faint, with the exception of the object J0005−28 (see Figure 8, displayed on a log–intensity scale). Unlike single slit spectra, with IFU data cubes, we are able to select the entire area of the H II region from which to extract the spectrum, and exclude the majority of the galaxy stellar background, resulting in better signal-to-noise. Test sample sizes showed that all the detectable H-alpha and [O III] in each H II region lay within the sample aperture, except where there are closely adjacent H II regions (e.g., J1609−04), where limiting the sample size to 6 arcsec diameter avoids sampling a different region. Ideally, single spaxel-based analysis would be preferable to multi-spaxel sampling, but these objects are so faint that the resultant noise is prohibitive.

Flux de-reddening was performed on the raw flux data using two methods. First, for consistency with other work, we used the dust reddening formulae from Cardelli et al. (1989) with $A_V = 3.1$, using the resultant Balmer line flux ratios as a check. To confirm these results, we used the dust models from Fischera & Dopita (2005), using a relative extinction curve with $R_V^A = 4.3$, where $R_V^A = A_V/(E_{B-V})$ and A_V is the V-band extinction. This is discussed in more detail in Vogt et al. (2013, Appendix 1). We used an initial Balmer decrement ratio of 2.82 for Hα/Hβ, corresponding to an electron temperature of 12,500 K, adjusted the electron temperature using the direct method derived from

the [O III] line ratios, then adjusted the apparent Balmer ratios by varying the value of A_V for the best fit to the Hγ/Hβ ratio, using the ratio Hδ/Hβ as a check, fitting to the Storey & Hummer (1995) Case B Balmer ratios. The de-reddened flux values reported in Table 2 are those using the Cardelli method. In all cases, the two approaches gave similar results (to within ∼3% in the de-reddened Balmer line ratios). In only one case, J2234−04, object A, did the de-reddening fail to provide a plausible result, and this has been excluded from the results reported here. It appears likely that two or more incompletely removed cosmic ray artefacts were the cause of the problem.

3. RESULTS

3.1. Hα Images

Images of the objects listed in Table 1 are shown in Figure 1. These are 38 × 25 arcsec Hα slices from the WiFeS data cubes. Spectra were extracted from these cubes using 6 arcsec diameter samples, centered on each (bright) H II region. Note that the seeing during the observations of object 7, J1403−27, was poor—3–5 arcsec—so the dimensions of the image do not indicate the true size of the H II region. The image scaling does not reflect the true brightness, but has been adjusted to illustrate the extent of the fainter parts of the H II regions. The sample size is larger than the worst seeing so avoids any sample size flux losses. In all but the one case the sample size is much larger than the object (see Table 1).

3.2. Spectra

Spectra extracted from the WiFeS data cubes are shown in Figures 2–7. The current data reduction pipeline creates a "sag" artefact for wavelengths shorter than ∼4000 Å, in the absence of a strong stellar continuum.[4] Stellar continua are weak or non-existent in most objects except for J0005−28, J2242−06, and J2349−42. Defective CCD chip amplification at the time of the observations caused two high noise regions in the spectrum of J2242−06, which have been replaced in Figure 3 with straight lines. Incipient noise from these two chip amplifiers is apparent in other spectra, but does not impact on any of the important diagnostic emission lines. De-reddened fluxes, equivalent widths, and logarithmic extinction coefficients (c(Hβ)) for the observed optical nebular lines are shown in Table 2. As noted in the Appendix, the extinction coefficients were calculated using the Cardelli reddening law with $A_V = 3.1$ Similar results (±3%) were obtained using methods derived from Fischera & Dopita (2005). The equivalent widths are large for some objects, indicating the very low continua, because the host galaxies are very small and faint, and the spectra were measured from an area sampling only the immediate area of the H II region.

Figure 5 is a close up of the spectra in Figures 2–4, from 4200 Å to 4500 Å, illustrating the Hγ and auroral [O III] 4363 Å lines. The signal-to-noise is mainly very good, but for three of the 14 objects in Figures 2–4, the detections are real but noisy (see Table 2).

---

[4] This is discussed in detail in Childress et al. (2013). It is an artefact of the data reduction pipeline that occurs for objects with very little stellar continuum, observed with the older WiFeS CCD detectors, whereby the spectrum "droops" at either end of the passband. It does not affect the flux measurements for individual emission lines. It is most evident in Figure 3, middle left panel.

Table 2
Reddening Corrected Line Fluxes Normalized to Hβ = 100, with Measured Hβ (erg s^{-1} cm^{-2} Å^{-1}), Equivalent Widths for Hα and Hβ, and Extinction Coefficient, c(Hβ)

			$I(\lambda)/I(H\beta) \times 100$			
Ion	J0005−28	J1118−17s2	J1152−02A	J1152−02B	J1225−06s2	J1328+02
[O II] 3726	90.39 ± 2.94	56.17 ± 16.48	119.11 ± 4.84	139.31 ± 6.67	77.69 ± 3.29	183.97 ± 7.56
[O II] 3729	117.91 ± 3.76	188.64 ± 20.45	171.01 ± 6.40	200.03 ± 8.49	108.84 ± 4.23	240.15 ± 9.24
[Ne III] 3869	39.98 ± 2.31	···	49.23 ± 1.48	46.29 ± 1.64	16.37 ± 0.96	20.30 ± 1.47
Hδ 4102	26.35 ± 0.86	28.45 ± 6.61	25.91 ± 0.84	26.31 ± 0.87	26.26 ± 1.13	23.95 ± 1.28
Hγ 4340	47.30 ± 1.47	35.79 ± 5.61	41.11 ± 1.29	42.75 ± 1.35	48.01 ± 1.61	46.40 ± 1.86
[O III] 4363	9.11 ± 0.32	···	6.82 ± 0.25	6.37 ± 0.26	4.83 ± 0.35	5.24 ± 0.49
Hβ 4861	100.00 ± 3.03	100.00 ± 5.28	100.00 ± 3.03	100.00 ± 3.05	100.00 ± 3.21	100.00 ± 3.30
[O III] 4959	150.49 ± 4.54	20.84 ± 2.67	172.31 ± 5.20	146.69 ± 4.46	62.66 ± 2.02	83.86 ± 2.89
[O III] 5007	451.97 ± 13.58	79.06 ± 4.51	517.38 ± 15.55	439.80 ± 13.24	190.32 ± 6.11	256.14 ± 8.06
[O I] 6300	2.69 ± 0.13	···	3.55 ± 0.13	3.73 ± 0.15	1.87 ± 0.41	···
[S III] 6312	1.62 ± 0.08	···	1.73 ± 0.07	1.76 ± 0.09	···	···
[N II] 6548	2.31 ± 0.11	···	2.25 ± 0.09	2.19 ± 0.10	···	3.36 ± 0.56
Hα 6563	279.20 ± 8.41	282.90 ± 10.21	282.48 ± 8.63	281.77 ± 8.50	277.53 ± 8.58	279.03 ± 8.87
[N II] 6584	4.76 ± 0.17	1.48 ± 1.63	6.99 ± 0.25	6.54 ± 0.25	4.05 ± 0.35	14.65 ± 0.94
[S II] 6716	11.92 ± 0.38	11.72 ± 1.82	15.64 ± 0.57	17.38 ± 0.58	11.85 ± 0.61	33.53 ± 1.41
[S II] 6731	8.76 ± 0.29	6.98 ± 1.67	11.29 ± 0.40	12.38 ± 0.43	8.27 ± 0.44	21.78 ± 1.11
Hβ 4861	8.52e-14	1.16E-15	2.90E-13	1.34E-13	2.10E-14	3.56E-15
EW(Hα)	685	717	1032	642	2482	234
EW(Hβ)	187	···	122	77.3	120	118
c(Hβ)	0.068	0.169	0.128	0.021	0.186	0.024
Ion	J1403−27	J1609−04(2)	J1609−04(5)	J2039−63A	J2039−63B	J2234−04B
[O II] 3726	122.74 ± 4.19	229.01 ± 10.05	209.89 ± 9.66	133.55 ± 5.98	75.86 ± 4.63	144.35 ± 7.89
[O II] 3729	165.52 ± 5.47	255.80 ± 10.86	230.35 ± 10.27	182.27 ± 7.44	103.61 ± 5.47	137.53 ± 7.69
[Ne III] 3869	38.81 ± 1.32	25.85 ± 2.04	30.13 ± 3.13	50.07 ± 2.42	38.62 ± 13.92	27.83 ± 18.80
Hδ 4102	27.67 ± 0.97	27.20 ± 1.67	20.43 ± 1.69	25.63 ± 1.25	24.68 ± 1.44	24.67 ± 2.00
Hγ 4340	48.07 ± 1.56	49.41 ± 2.04	48.30 ± 2.18	49.77 ± 1.85	48.82 ± 2.25	40.75 ± 2.15
[O III] 4363	7.66 ± 0.32	2.27 ± 0.39	6.10 ± 1.09	9.72 ± 0.55	8.39 ± 0.91	6.41 ± 0.93
Hβ 4861	100.00 ± 3.09	100.00 ± 3.47	100.00 ± 3.49	100.00 ± 3.21	100.00 ± 3.27	100.00 ± 3.78
[O III] 4959	142.26 ± 4.33	91.29 ± 3.11	110.15 ± 3.77	172.74 ± 5.34	156.84 ± 5.05	118.89 ± 4.31
[O III] 5007	420.32 ± 12.66	266.71 ± 8.41	322.78 ± 10.14	502.15 ± 15.21	462.63 ± 14.22	351.19 ± 11.35
[O I] 6300	3.66 ± 0.18	5.66 ± 0.46	6.65 ± 0.56	5.32 ± 0.32	2.79 ± 0.51	···
[S III] 6312	1.97 ± 0.12	0.00 ± 0.00	···	1.83 ± 0.21	···	···
[N II] 6548	2.32 ± 0.15	6.18 ± 0.60	4.96 ± 0.51	2.76 ± 0.25	···	···
Hα 6563	280.10 ± 8.52	285.58 ± 9.95	279.82 ± 8.72	279.63 ± 8.55	280.15 ± 8.72	280.09 ± 9.14
[N II] 6584	7.69 ± 0.31	11.92 ± 0.60	12.58 ± 0.79	8.65 ± 0.43	5.69 ± 0.57	7.87 ± 0.85
[S II] 6716	19.52 ± 0.69	29.77 ± 1.15	27.18 ± 1.17	19.11 ± 0.75	12.29 ± 0.66	17.05 ± 1.17
[S II] 6731	13.87 ± 0.52	20.96 ± 0.89	18.69 ± 0.91	14.22 ± 0.60	8.19 ± 0.68	12.28 ± 1.09
Hβ 4861	9.07E-14	1.57E-14	1.72E-14	2.52E-14	7.05E-15	2.39E-15
EW(Hα)	286	215	157	301	459	···
EW(Hβ)	66.2	77.6	48.1	69.5	150	···
c(Hβ)	0.216	0.448	0.619	0.219	0.028	0
Ion	J2242−06	J2254−26	J2311−42A	J2311−42B	J2349−22	
[O II] 3726	132.13 ± 6.17	66.71 ± 2.46	137.44 ± 7.49	92.28 ± 3.86	113.10 ± 5.82	
[O II] 3729	180.06 ± 7.60	83.32 ± 2.95	206.55 ± 9.57	106.01 ± 4.27	155.67 ± 7.10	
[Ne III] 3869	28.65 ± 1.89	55.79 ± 1.83	36.57 ± 2.56	51.11 ± 2.01	34.21 ± 2.53	
Hδ 4102	26.87 ± 1.45	25.74 ± 0.87	30.15 ± 1.93	27.72 ± 1.20	22.54 ± 1.79	
Hγ 4340	44.07 ± 1.76	46.15 ± 1.47	51.15 ± 2.21	47.21 ± 1.70	44.22 ± 2.12	
[O III] 4363	5.07 ± 0.63	10.11 ± 0.39	5.61 ± 0.80	9.45 ± 0.54	4.87 ± 0.97	
Hβ 4861	100.00 ± 3.26	100.00 ± 3.05	100.00 ± 3.52	100.00 ± 3.25	100.00 ± 3.48	
[O III] 4959	99.31 ± 3.23	224.02 ± 6.75	133.40 ± 4.54	192.18 ± 5.94	95.81 ± 3.39	
[O III] 5007	297.31 ± 9.17	680.52 ± 20.45	397.17 ± 12.70	569.46 ± 17.26	272.65 ± 8.75	
[O I] 6300	3.54 ± 0.59	1.82 ± 0.10	2.37 ± 0.58	2.39 ± 0.23	3.31 ± 0.37	
[S III] 6312	···	1.89 ± 0.09	0.00 ± 0.00	2.45 ± 0.27	1.18 ± 0.31	
[N II] 6548	···	1.74 ± 0.09	5.09 ± 0.74	1.90 ± 0.20	3.05 ± 0.39	
Hα 6563	280.60 ± 8.82	281.58 ± 8.50	281.95 ± 9.12	280.83 ± 8.56	280.33 ± 9.32	
[N II] 6584	8.60 ± 0.38	5.32 ± 0.20	11.86 ± 0.82	6.42 ± 0.35	6.32 ± 0.46	
[S II] 6716	23.75 ± 1.19	9.01 ± 0.31	23.58 ± 1.11	14.28 ± 0.58	18.54 ± 0.84	
[S II] 6731	15.87 ± 0.95	6.84 ± 0.24	16.01 ± 0.89	9.80 ± 0.45	12.73 ± 0.67	
Hβ 4861	1.13E-14	7.17E-14	8.78E-15	2.10E-14	8.85E-15	
EW(Hα)	211	811	1982	631	103	
EW(Hβ)	47.9	177	710	106	30	
c(Hβ)	0	0.071	0.180	0.127	0.115	

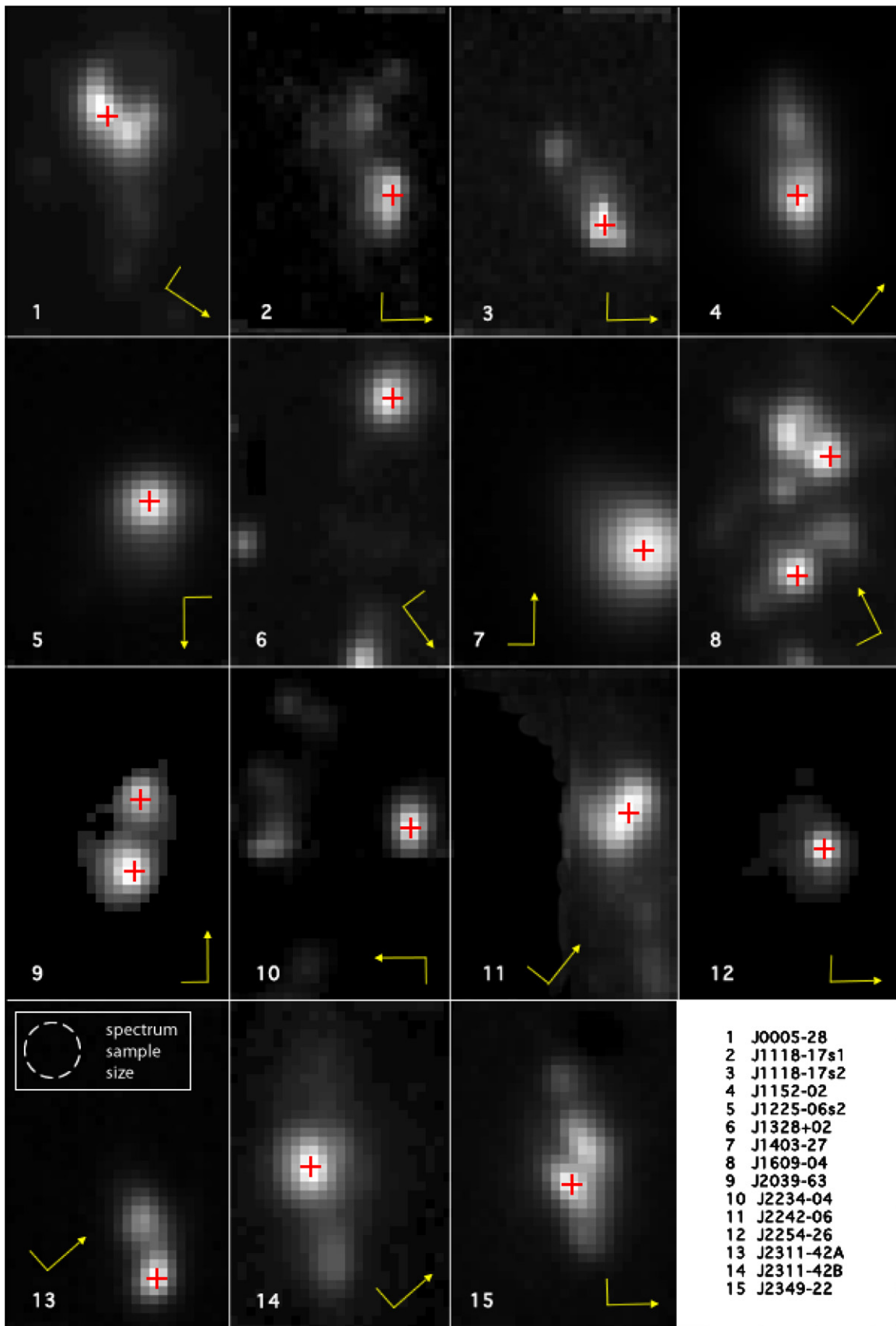**Note.** For a discussion of the errors, see the Appendix.

Figure 1. Hα slices from WiFeS 35 × 28 arcsec image cubes. The size of the areas sampled to extract spectra is shown in panel 13. North is indicated by the long arrow and east by the bar (±15°). The red crosses mark the center of the sampled areas. Note that the images have been stretched to show the fainter areas.

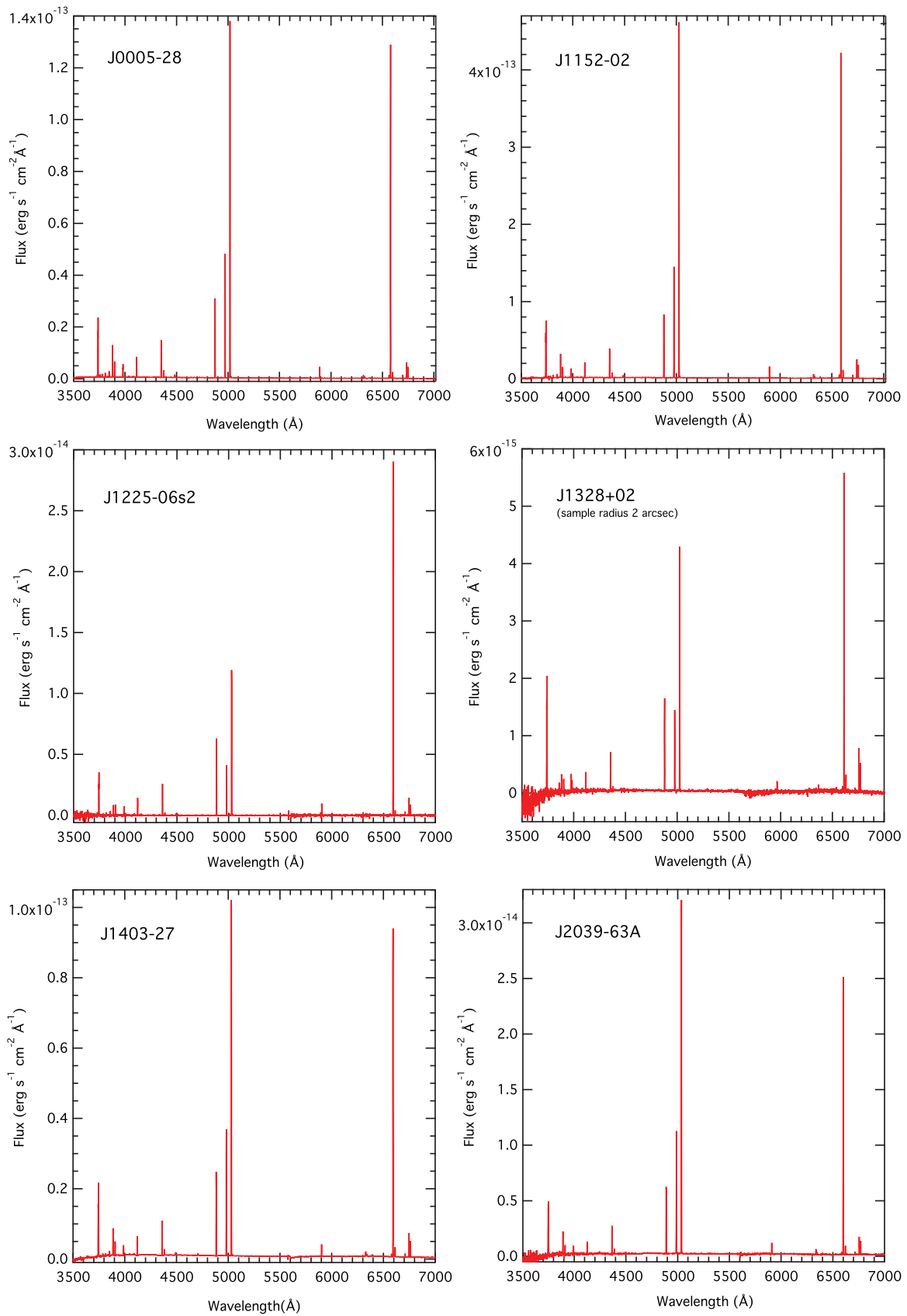(A color version of this figure is available in the online journal.)

Figure 2. Spectra for J0005−28, J1152−02, J1225−06s2, J1328+02, J1403−27, and J2039−63A.

(A color version of this figure is available in the online journal.)
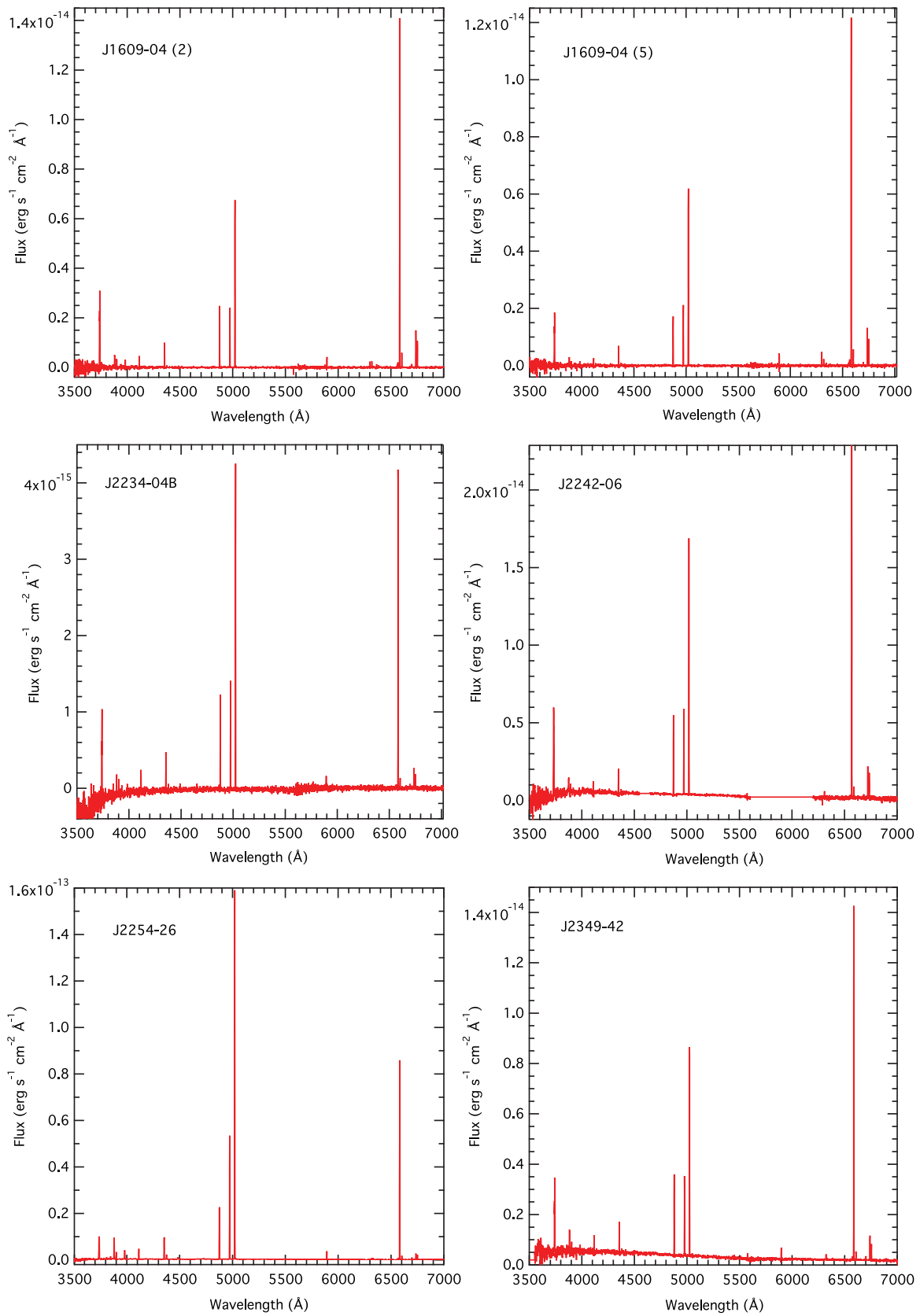
Figure 3. Spectra for J1609−04(2), J1609−04(5), J2234−04B, J2242−06, J2254−26, and J2349−42.

(A color version of this figure is available in the online journal.)
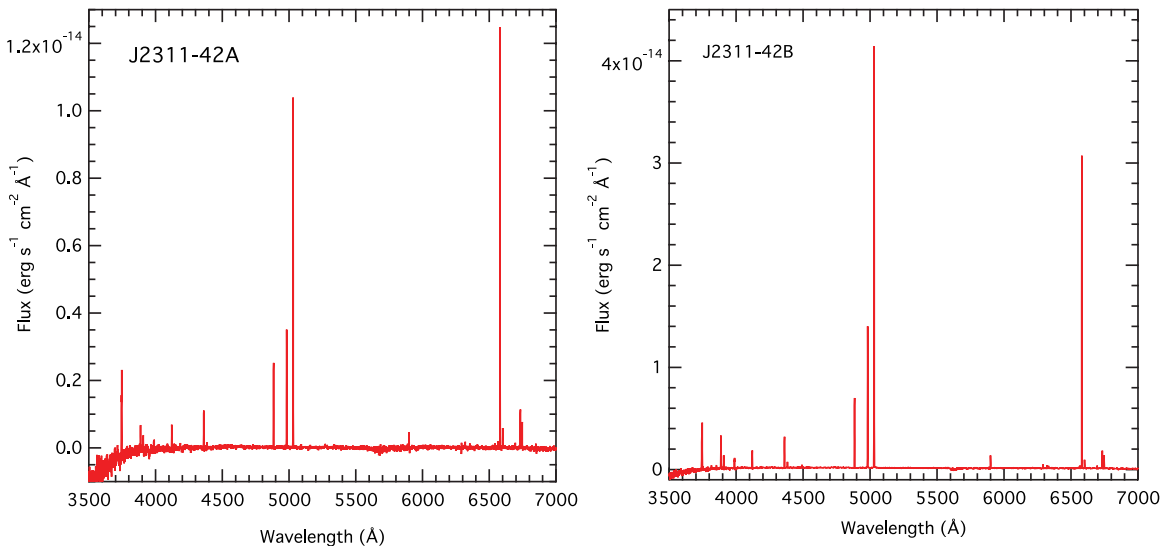
Figure 4. Spectra for J2311−42A and J2311−42B.
(A color version of this figure is available in the online journal.)

3.3. Notes on Particular Objects

The spectrum from J1118−17s2 is shown in Figure 6. An enlarged section of the spectrum of J1118−17s2 near Hα is shown in Figure 7, illustrating the apparent absence (to within the noise) of [N II], although both [S II] lines are apparent. This lack of any evidence for nitrogen suggests a particularly low metallicity, which we have estimated below using strong-line diagnostic measurements. This object (and the associated J1118−17s1) warrants further observation to reduce the noise and establish the [N II] flux. We have not presented the spectrum of J1118−17s1 as the signal-to-noise ratio was very poor and did not permit reliable measurement of any fluxes other than Hα, Hβ and [O III] 5007 Å. Figure 8 shows the emission line rich spectrum of the bright BCD J0005−28 with flux on a logarithmic scale. Twelve Balmer lines can be seen, allowing particularly accurate de-reddening to be calculated. The de-reddening process based on the Hα to Hβ ratio gave ratios to within 0.3% for Hδ and 12% for Hϵ of the expected values for Case B.

4. NEBULAR METALLICITIES

4.1. Electron Temperatures and Oxygen Abundances

The electron temperature, T_e, can be derived from collisionally excited line fluxes, for a variety of ionic species, provided the auroral line is observed (in the case of O III, the 4363 Å line). The method most frequently used makes use of the ratio of fluxes of the bright [O III] lines to the auroral line. This is a well-established technique (see discussions in Osterbrock & Ferland 2006; Nicholls et al. 2013), but it calculates only the O++ abundance, not the total gas-phase abundance of oxygen. In most H II regions, the contributions to total oxygen from neutral O and O+++ are minor, so in addition to O++ we only need to calculate the contribution from O+.

If the equivalent auroral lines for [O II], [N II] and [S III] are present in the spectra, the electron temperatures can be calculated using these lines too, and since they peak at different regions in the H II region, the auroral lines collectively sample the complete volume. When these auroral lines are not observed, empirical methods can be used to estimate the O+ abundance, for

example in Izotov et al. (2006, Equations (3) and (4)). However, as those authors note, the methods depend on having reliable atomic data (energy levels, transition probabilities, and collision strengths). Consequently we have approached the problem again from first principles, using the latest atomic data, to derive the total oxygen abundance.[5]

The rate of collisional excitation for O++ from the ^3P ground state(s) to the $^1D_2$ level is given, for the thermal equilibrium case (Nicholls et al. 2012), by,

$$r_{12} = n_e n_{O^{++}} \left(\frac{h^2 \sqrt{2}}{4\pi^{3/2} m_e^{3/2} \sqrt{k_B}} \right) \frac{1}{g_1 T_e} \Upsilon_{12}(T) \exp\left(-\frac{E_{12}}{k_B T_e} \right),$$

(1)

where h is the Planck constant, m_e is the electron mass, g_1 is the statistical weight of the ground state (= 9 for O++), k_B is the Boltzmann constant, Υ_{12} is the net effective collision strength for collisional excitations from the ground ^3P states to the $^1D_2$ state and E_{12} is the energy level of the $^1D_2$ state. Ignoring the small contribution to the population of the $^1D_2$ level from radiative cascade from higher energy levels, the rate of emission of photons from that level is equal to the rate of excitation, i.e., $r_{12} = r_{21}$. The emissivity of [O III] from transitions from the $^1D_2$ (λλ 5007, 4959 and 4931) level is proportional to $r_{21} \times E_{12}$. Here we have used the total effective collision strengths for the forbidden $^1D_2$ to ^3P transitions, so we use the flux-weighted photon energy, corresponding to a wavelength of 4997 Å, for E_{12}.

The emissivity of Hβ is proportional to $n_e \times n_{H^+} \times \alpha_B^{\mathrm{eff}}(H_\beta)$ (Dopita & Sutherland 2003), where n_e is the electron density, n_{H^+} is the ionized hydrogen density, and $\alpha_B^{\mathrm{eff}}(H_\beta)$ is the effective emissivity for Hβ, which takes into account photon energies and branching ratios, and for which values have been computed by Storey & Hummer (1995).

Given that the ratio of the flux of [O III] to that of Hβ is equal to the ratio of their emissivities multiplied by their photon energies, for a given geometry, one may reorganise the above equations to derive an expression for the ratio of the number

---

[5] In this work, we do not have data for the [O II] λλ7320,30 lines, so the Izotov method provides a useful comparison.
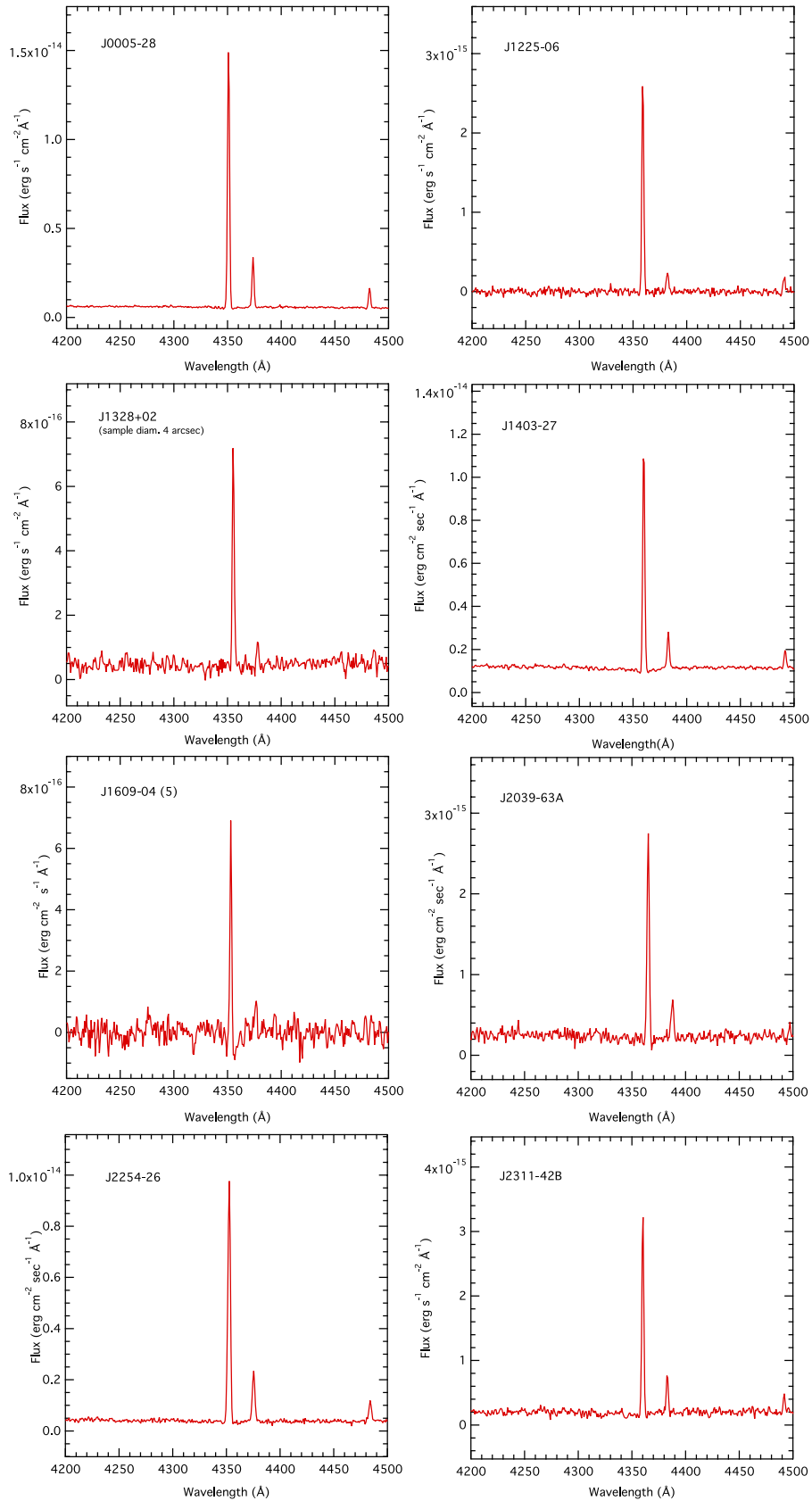
Figure 5. Close up of the Hγ and [O III] 4363 Å lines for eight of the SIGRID objects.

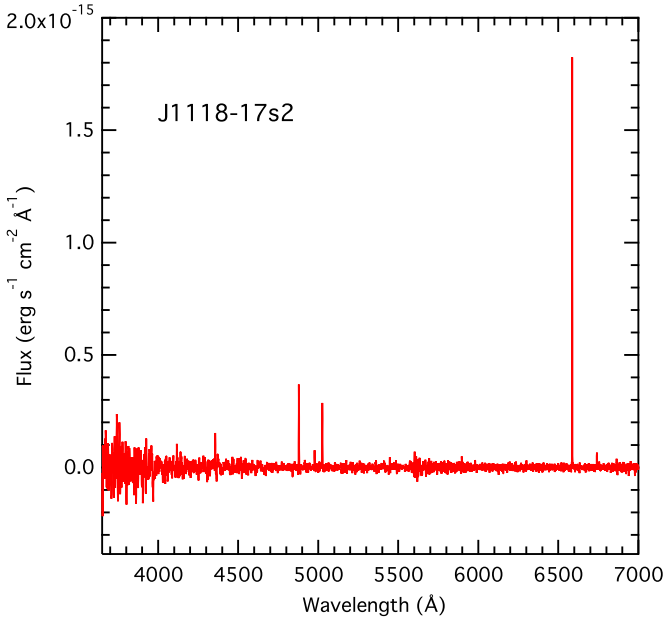(A color version of this figure is available in the online journal.)

Figure 6. Spectrum for J1118−17s2 (pipeline "sag" removed).
(A color version of this figure is available in the online journal.)

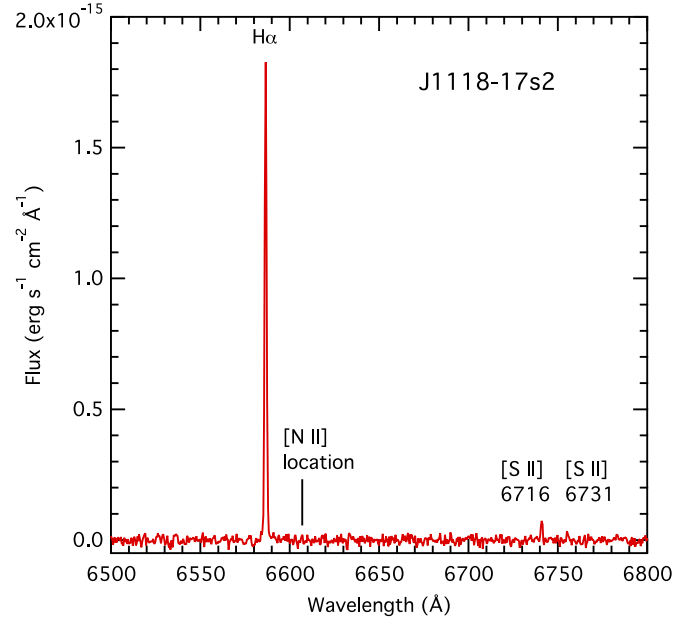**Figure 7.** Section of spectrum for J1118−17s2, showing apparent absence of any [N II] emission lines.
(A color version of this figure is available in the online journal.)

density of O^{++} ions to hydrogen ions (i.e., the O^{++} abundance) in terms of the flux ratio of [O III]($^1D_2$) to H_β,

$$\frac{n_{O^{++}}}{n_{H^+}} = \frac{\text{flux}(O^{++})}{\text{flux}(H_\beta)} \cdot g_1 \cdot \sqrt{T_e} \cdot \alpha_B^{\text{eff}}(H_\beta) \cdot \exp(E_{12}/(kT_e))$$
$$\times 115885.4/(E_{12} \cdot \Upsilon_{12}), \quad (2)$$

where T_e is the electron temperature derived from the [O III] line ratio, for which there is a simple expression from Nicholls et al. (2013),

$$T_e = a(-\log_{10}(\mathcal{R}) - b)^{-c}, \quad (3)$$

where, for [O III],

$$\mathcal{R} = \frac{j(\lambda 4363)}{j(\lambda 5007) + j(\lambda 4959)}, \quad (4)$$

and $a = 13229$, $b = 0.92350$, and $c = 0.98196$.

In an identical fashion, one may derive an expression for the abundance of O II using the observed fluxes from the [O II] 3726,3729$\lambda\lambda$ lines,

$$\frac{n_{O^+}}{n_{H^+}} = \frac{\text{flux}(O^+)}{\text{flux}(H_\beta)} \cdot g_{1(O^+)} \cdot \sqrt{T_e} \cdot \alpha_B^{\text{eff}}(H_\beta) \cdot \exp(E_{12(O^+)}/(kT_e))$$
$$\times 115885.4/(E_{12(O^+)} \cdot \Upsilon_{12(O^+)}), \quad (5)$$

where, in this case, T_e is the electron temperature derived from the [O II] ratio (see Nicholls et al. 2013) using the ratio of the 7320,30$\lambda\lambda$ lines to the 3726,3729$\lambda\lambda$ lines. If, as in the case of these observations, the NIR lines are not available, it is possible to derive an expression for the [O II] electron temperature from the Mappings photoionization models as a polynomial in terms of *total* gas-phase oxygen abundance,

$$T_e([\text{O II}]) = T_e([\text{O III}])$$
$$\times (3.0794 - 0.086924Z - 0.1053Z^2 + 0.010225Z^3), \quad (6)$$

where $Z = 12 + \log(\text{O/H})$.

This does not provide the final answer, and it is necessary to iterate to a final value for the abundance of O^+, starting by using the O^{++} abundance as the total oxygen abundance. The process converges in less that five iterations. Garnett (1992) and López-Sánchez et al. (2012) have used a simpler approach, expressing the low ionization zone temperature (effectively the [O II] temperature) in terms of the [O III] temperature, which does not require iteration. Garnett (1992) used a linear relation, whereas López-Sánchez et al. (2012) used a more complex fit to photoionization model data.

Equation (7) shows the expression used by López-Sánchez et al. (2012):

$$T_e(\text{O II}) = T_e(\text{O III}) + 450 - 70 \times \exp[(T_e(\text{O III})/5000)^{1.22}]. \quad (7)$$

Equation (7) gives total oxygen abundance values close to those from iterating Equation (6). Values determined for oxygen abundances are not exact, because of the nature of the approximations used, the calculated values for oxygen abundances depend on the photoionization models used to build the models, and the use of a model derived from a single value of the ionization parameter, q. Testing the two methods (Equations (6) and (7)) against artificial data indicates that they generate total oxygen abundances within 1% of the input values. The iterative approach (Equation (5)) is marginally the more consistent of the two over a range of ionization parameter values.

The above equations may be simplified for computation by using accurate expansions in terms of the [O III] electron temperature to $\alpha_B^{\text{eff}}(H_\beta)$, $\Upsilon(^1D_2)$, and $\Upsilon(^2D^0_{3/2,5/2})$. The Case B emissivity data for H_β as a function of temperature, from Storey & Hummer (1995) may be fit with a simple power law,

$$\alpha_B^{\text{eff}}(H_\beta) = -1.7221e{-26} + 1.4772e{-22} \times T_e^{-0.75538}. \quad (8)$$

The effective collision strengths for the O^{++} $^1D_2$ level (Palay et al. 2012), from which the $\lambda\lambda 4959, 5007$ doublet originates, can be fit with a simple exponential function of temperature,

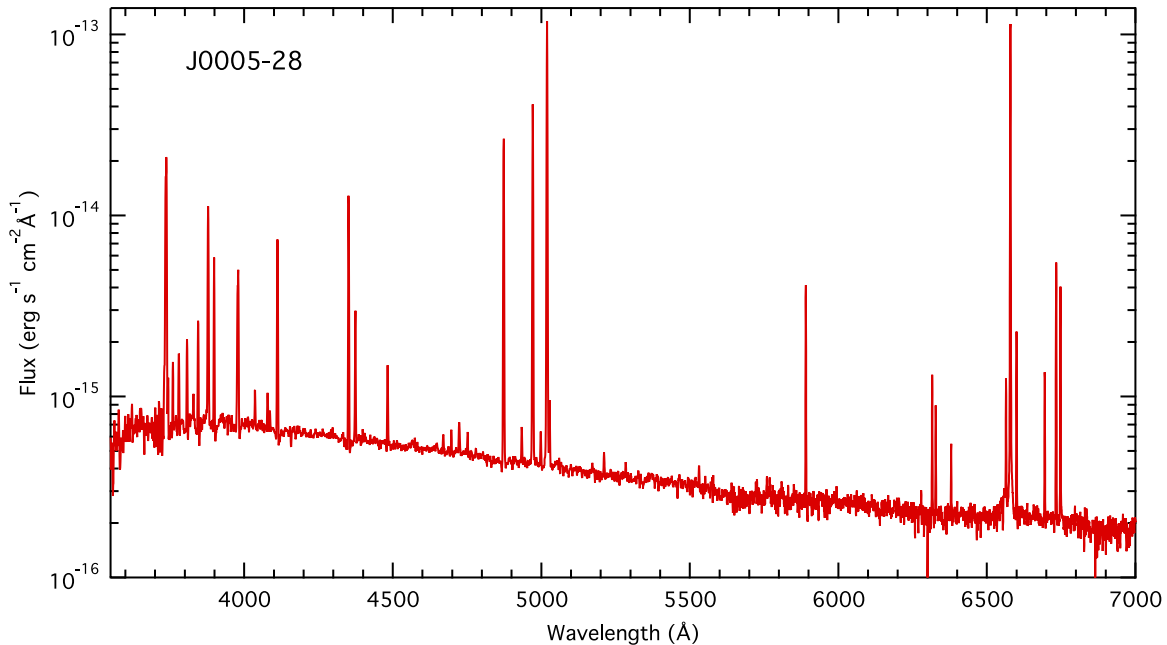$$\Upsilon(^1D_2) = 3.0733 - 0.94563 \times \exp((5000 - T_e)/12105), \quad (9)$$

Figure 8. Spectrum of J0005−28, log flux axis. Several Balmer lines are apparent, and the [O III] 4363 Å line is strong.

(A color version of this figure is available in the online journal.)

and the effective collision strengths for O^{++} from Tayal (2007) for the composite upper state, $^2D^0_{3/2,5/2}$, from which the $\lambda\lambda 3726,9$ doublet originates, can similarly be fit by a linear function of temperature,

$$\Upsilon\left(^2D^0_{3/2,5/2}\right) = 1.3394 + 1.3443\mathrm{e}{-06} \times T_e. \qquad (10)$$

Applying these methods to the present observations, we obtain the electron temperatures and total gas-phase oxygen abundances shown in Table 4. The values for J1118−16s2 are not listed as the $\lambda 4363$ line was not observed. The uncertainties in T_e were calculated from the flux error values, in Equation (3), and propagated through to the abundance values. See the Appendix for a discussion of the error estimation.

4.2. Strong-line Diagnostic Grids

There are two principal methods for determining oxygen abundances from H II region optical spectra, the direct or electron temperature (T_e) method and the strong-line methods. The T_e method is possible if one of the auroral lines is observed at adequate signal-to-noise ($>3\sigma$), usually [O III] 4363 Å. This is the case in all but one of the galaxies discussed here and is detailed below. The so-called strong-line methods use flux ratios of the prominent nebular lines to determine abundances (e.g., Dopita et al. 2013; Kewley & Dopita 2002; Kewley & Ellison 2008). Conventionally, the strong-line methods were empirical, calibrated against results using the direct method. However, recently, Dopita et al. (2013) have extensively revised the strong-line techniques, developing diagnostic grids based on the Mappings photoionization modeling code, using the latest atomic data, and the possibility that the electrons exhibit a non-equilibrium κ energy distribution (Nicholls et al. 2012, 2013). The grids are new, and the ratios used have been selected to maximize the orthogonality of the parameters, avoiding to a large extent the degeneracy of older diagnostics, and to solve for both metallicity and ionization parameter. These new diagnostics generate values for both the oxygen abundance and

the ionization parameter, q, and give substantially more consistent abundance values than the older methods. This can be seen by comparing the metallicity results for the different diagnostics from Table 3 and the older diagnostic results listed in Table 4. In Table 3, the diagnostics involving the ratio [N II]/[S II] and [N II]/[O II] are particularly consistent, differing by typically <0.03 dex.

The ionization parameter q (sometimes expressed as $U = q/c$, where c is the speed of light) is the ratio of the number of ionizing source photons passing through a unit volume to the neutral hydrogen density. The photon flux matches the number of new ions it produces, and as q has the dimensions of velocity, it can be understood as the maximum speed at which the boundary of the ionized region can move outward (Dopita & Sutherland 2003). q is at its maximum at the inner edge of the ionized region of an H II region, and falls to zero at the outer edge of the ionized nebula, where the ionizing flux is fully depleted. A problem with older diagnostics such as R_{23} is that measured metallicities depend on the ionization parameter. There have been previous attempts to solve for the ionization parameter (McGaugh 1994; Kewley & Dopita 2002; Pilyugin & Thuan 2005) but these new diagnostics solve for its value independently of the metallicity, and consequently, take into account the ionization gradients present in H II regions. The diagnostics chosen here are also relatively insensitive to non-equilibrium (κ) electron energy distributions, especially for values of $\kappa > 20$. In addition, κ distributions have a smaller effect on the excitation of lower metallicity H II regions than in higher metallicity objects. For this reason, and in the interests of clarity, we present here only the equilibrium (Maxwell–Boltzmann, or $\kappa = \infty$) results.

Figures 9 and 10 plot the log flux ratios for the observed objects on the diagnostic grids from Dopita et al. (2013). Not all of the objects can be accommodated within these grids. There are several possible reasons, and these will be discussed in detail in the second paper in this series. One likely cause relates to electron densities. The grids shown here are calculated for an electron density, $n_e \sim 5$ cm^{-3}. For the majority of the observed objects, this is accurate, but for some the densities are somewhat

11

Table 3
Metallicity Results from Strong-line Grids for $\kappa = \infty$

Diagnostic:	N II/S II vs. O III/S II	N II/S II vs. O III/Hb	N II/O II vs. O III/O II	N II/O II vs. O III/S II	N II/S II vs. O III/O II	N II/O II vs. O III/Hb	N II/Ha vs. O III/Hb	N II/Ha vs. O III/O II
J0005−28								
z	8.012	–	8.0428	8.0355	8.0114	–	8.1191	8.1011
log(q)	7.6328	–	7.7212	7.6596	7.6845	–	7.9568	7.7802
mean z	8.012 ± 0.000							
mean log(q)	7.659 ± 0.037							
J1118−17s2								
Z	–	–	–	–	–	–	7.5448	7.4741
log(q)	–	–	–	–	–	–	6.9500	6.7092
mean z	7.509 ± 0.050							
mean log(q)	6.830 ± 0.170							
J1152−02A								
z	8.0896	–	8.0762	8.0736	8.0868	–	–	8.198
log(q)	7.5707	–	7.5506	7.5611	7.558	–	–	7.6697
mean z	8.088 ± 0.002							
mean log(q)	7.564 ± 0.009							
J1152−02B								
z	7.9802	–	7.8965	7.9038	7.9819	–	8.1878	8.118
log(q)	7.3404	–	7.2459	7.3072	7.2869	–	7.7019	7.3713
mean z	7.981 ± 0.001							
mean log(q)	7.314 ± 0.038							
J1225−06s2								
z	7.9289	7.9321	7.9924	7.9891	7.9256	7.9736	7.9106	7.9261
log(q)	7.1382	7.0849	7.1958	7.157	7.1611	7.0573	7.0925	7.1651
mean z	7.929 ± 0.003							
mean log(q)	7.128 ± 0.039							
J1328+02								
z	8.1465	8.1159	8.2471	8.2413	8.1337	8.2524	8.3003	8.2909
log(q)	6.9894	7.1697	7.0976	7.0408	7.0481	7.1428	7.0164	7.123
mean z	8.132 ± 0.015							
mean log(q)	7.069 ± 0.092							
J1403−27								
z	8.0137	8.0161	8.1393	8.1363	8.0106	–	8.2286	8.1978
log(q)	7.2684	8.045	7.4556	7.343	7.3739	–	7.5551	7.4934
mean z	8.013 ± 0.003							
mean log(q)	7.562 ± 0.421							
J1609−04(2)								
z	8.0654	8.0303	8.0418	8.0447	8.0681	8.0722	8.243	8.1959
log(q)	6.992	7.2226	6.9825	6.9856	6.9843	7.2026	–	7.0429
mean z	8.055 ± 0.021							
mean log(q)	7.066 ± 0.135							
J1609−04(5)								
z	8.1435	8.1261	8.1628	8.1616	8.1424	8.1753	8.3091	8.2626
log(q)	7.1225	7.3364	7.1189	7.1261	7.129	7.3023	7.1813	7.182
mean z	8.137 ± 0.010							
mean log(q)	7.196 ± 0.122							
J2039−63A								
z	8.0889	–	8.1589	8.1578	8.0853	–	8.35	8.2661
log(q)	7.4083	–	7.5284	7.4515	7.4722	–	8.3704	7.6159
mean z	8.087 ± 0.003							
mean log(q)	7.440 ± 0.045							
J2039−63B								
z	8.1379	8.1515	–	8.2147	–	–	8.1677	–
log(q)	7.7838	8.127	–	7.9763	–	–	7.9284	–
mean z	8.145 ± 0.010							
mean log(q)	7.955 ± 0.243							
J2234−04B								
z	8.1115	8.1104	8.1667	8.1643	8.1079	8.1659	8.1713	8.1742
log(q)	7.3037	7.4352	7.368	7.3359	7.3459	7.3929	7.0618	7.3863
mean z	8.110 ± 0.002							
mean log(q)	7.362 ± 0.067							

Table 3
(Continued)

Diagnostic:	N II/S II vs. O III/S II	N II/S II vs. O III/Hb	N II/O II vs. O III/O II	N II/O II vs. O III/S II	N II/S II vs. O III/O II	N II/O II vs. O III/Hb	N II/Ha vs. O III/Hb	N II/Ha vs. O III/O II
J2242−06								
z	7.9952	7.9712	8.1484	8.1391	7.9836	8.15	8.16	8.1612
log(q)	7.0778	7.3706	7.2361	7.1386	7.1563	7.2384	6.7332	7.2408
mean z	7.983 ± 0.012							
mean log(q)	7.202 ± 0.152							
J2254−26								
no results								
J2311−42A								
z	8.1817	8.1705	8.2661	8.2633	8.1760	–	8.3488	8.3167
log(q)	7.2614	7.5276	7.3981	7.3311	7.3515	–	7.5032	7.4314
mean z	8.176 ± 0.006							
mean log(q)	7.380 ± 0.135							
J2311−42B								
z	8.1222	–	–	8.2207	–	–	–	–
log(q)	7.8286	–	–	8.1406	–	–	–	–
mean z	8.171 ± 0.049							
mean log(q)	7.985 ± 0.156							
J2349−22								
z	7.9360	7.9091	8.0443	8.0398	7.9293	8.0464	8.0732	8.0699
log(q)	7.1122	7.3623	7.2168	7.1481	7.1602	7.2239	6.656	7.2224
mean z	7.925 ± 0.014							
mean log(q)	7.212 ± 0.133							

Notes. The diagnostic grids are described in detail in Dopita et al. (2013). The uncertainties quoted are based on the variance of the average values for the first five diagnostics listed here. "–" indicates the diagnostic does not return a value for abundance or ionization parameter.

Table 4
[O III] Electron Temperatures and Gas-phase Oxygen Abundances

Object	T_e	Zs[a]	Z	Z(grids)[b]	δZ[c]	Old Strong Line[d]			
	(K)	(this work)	(Izotov06)			M91	KK04	PP04	PP04
								5007.N2	N2
J0005−28	14720 ± 36	7.847 ± 0.025	7.858	8.012	0.165	8.104	8.306	7.954	7.951
J1152−02A	12249 ± 34	8.151 ± 0.025	8.178	8.088	−0.063	8.297	8.466	7.988	8.034
J1152−02B	12723 ± 55	8.094 ± 0.026	8.108	7.981	−0.113	8.288	8.455	8.001	8.021
J1225−06s2	16560 ± 395	7.498 ± 0.028	7.462	7.929	0.431	7.750	7.999	8.053	7.910
J1328+02	14847 ± 464	7.867 ± 0.027	7.835	8.132	0.265	8.234	8.397	8.190	8.165
J1403−27	14022 ± 71	7.939 ± 0.025	7.942	8.013	0.074	8.199	8.381	8.031	8.054
J1609−04b2	10432 ± 491	8.345 ± 0.026	8.393	8.055	−0.290	8.323	8.471	8.152	8.127
J1609−04b5	14235 ± 984	7.959 ± 0.028	7.944	8.137	0.178	8.313	8.468	8.136	8.140
J2039−63A	14384 ± 182	7.965 ± 0.027	7.976	8.087	0.121	8.321	8.485	8.023	8.076
J2039−63B	13984 ± 499	7.894 ± 0.029	7.911	8.145	0.251	8.066	8.276	7.976	7.992
J2234−04B	14024 ± 754	7.897 ± 0.032	7.890	8.110	0.213	8.118	8.312	8.059	8.058
J2242−06	13625 ± 575	7.921 ± 0.027	7.906	7.983	0.062	8.109	8.300	8.094	8.074
J2254−26	12871 ± 43	8.090 ± 0.025	8.129	⋯	⋯	8.250	8.433	7.912	7.976
J2311−42A	12584 ± 580	8.090 ± 0.029	8.100	8.176	0.086	8.254	8.425	8.098	8.129
J2311−42B	13453 ± 160	8.011 ± 0.027	8.038	8.171	0.160	8.217	8.403	7.963	8.018
J2349−22	13837 ± 1054	7.858 ± 0.029	7.839	7.925	0.067	8.015	8.222	8.064	8.015

Notes.
[a] Z(this work) derived from Equations (2), (5), and (6).
[b] The Z(grids) values are the average of the new grids involving the log(N II/S II) and log(N II/O II) ratios.
[c] δZ is the difference between Z(grids) and Z(this work).
[d] Older strong-line methods (Columns 7–10) described in Kewley & Ellison (2008).

higher. Below we analyze the ratios of the two [S II] lines (6716 and 6731 Å) which are a useful diagnostic of electron density (Osterbrock & Ferland 2006), and it is clear that some of the objects exhibit higher densities. Some of the "misfit" points can be accommodated on grids calculated for higher electron densities (see below and Figure 12).

4.3. Strong-line Metallicities

Table 3 lists the oxygen abundances and ionization coefficients computed from the new diagnostic grids using the "pyqz" interpolation described in Dopita et al. (2013). While the interpolation scheme does not always work reliably for near-vertical
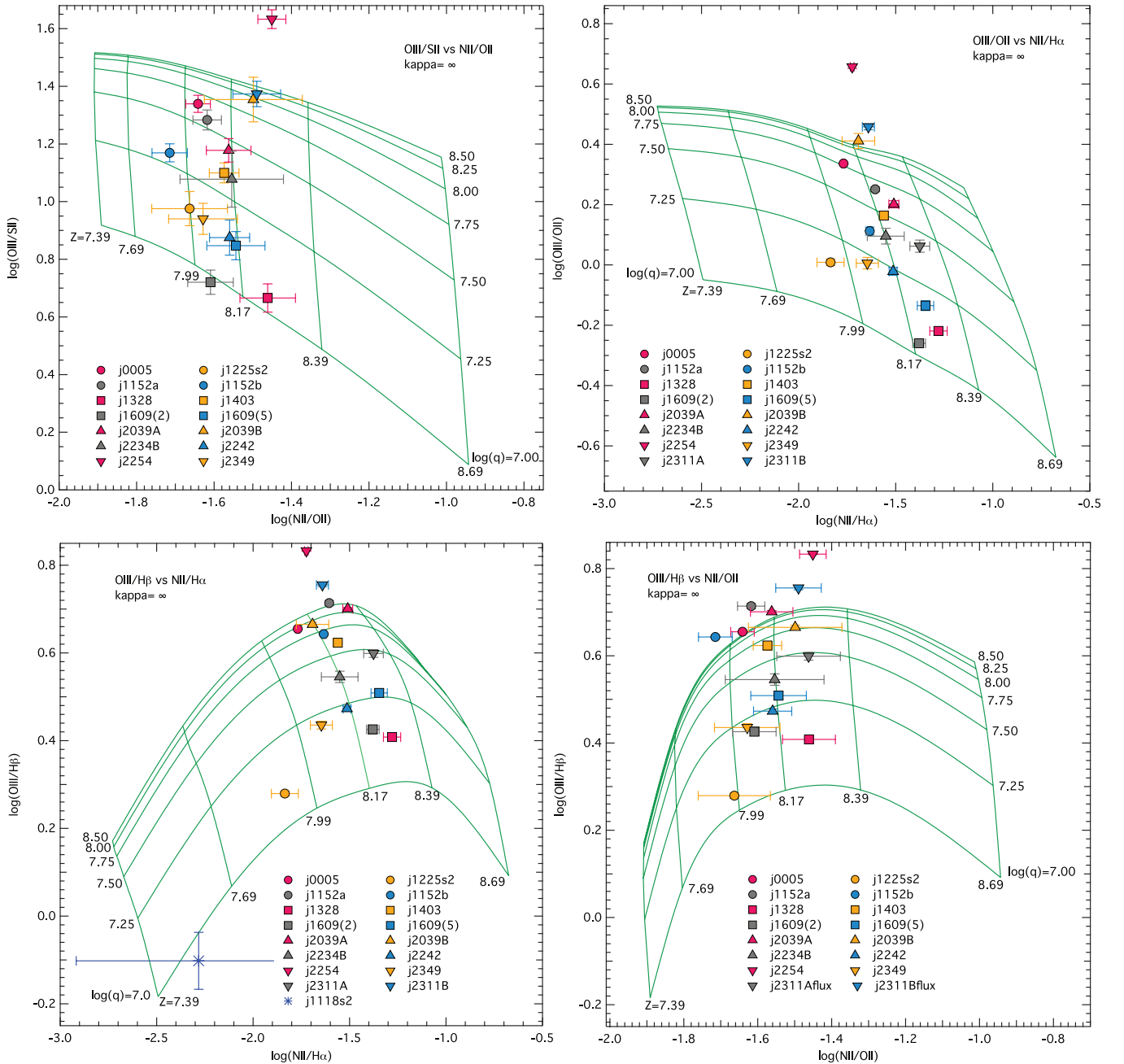
Figure 9. Observed flux ratios for SIGRID objects plotted on the O III/S II–N II/O II, O III/O II–N II/Ha, O III/Hb–N II/Ha and O III/Hb–N II/O II grids.
(A color version of this figure is available in the online journal.)

grid lines, leading to null results, it is clear that different diagnostics yield somewhat different results. However, the consistency is far better than earlier methods permitted. We have found that for low metallicity objects ($<0.5\,Z_\odot$), diagnostics listed in Table 3 involving $\log(\mathrm{N\,II/S\,II})$ give values for the metallicity that differ by typically less than 0.02 dex and diagnostic using the $\log(\mathrm{N\,II/O\,II})$ ratios are similar. It is also evident from Table 3 that the direct methods are nearly all lower by $\sim$0.13 dex than the best $\log(\mathrm{N\,II/S\,II})$ strong-line diagnostic values. This is in agreement with the findings of López-Sánchez et al. (2012) that the direct method abundances are generally lower than strong-line estimates. However, with the newer atomic data, the recalculated direct method abundances, and the revised Mappings photoionization code, these differences are smaller. For comparison we also present the results of older strong-line di-

agnostics, in Table 4. Perhaps the most variable result is that for J1118−17s2. This is not surprising, as the [N II] flux is poorly defined. It appears likely that an oxygen abundance figure of $\sim$7.2 ($\sim Z_\odot/30$) is a reasonable estimate.

It is worth noting that the Mappings photoionization modeling grids used here take into account the total oxygen abundance, i.e., both the gas-phase oxygen and that incorporated in dust grains. When comparing the electron temperature and strong-line abundances, it is necessary to increase the electron temperature oxygen abundance values by $\sim$0.07dex, to allow for the oxygen in dust grains that the direct method does not account for. This, of course, assumes a particular level of dust in the interstellar medium (ISM). In the Mappings strong-line diagnostic grids, we assume a 1.0 solar dust depletion. Rémy-Ruyer et al. (2014) found that the gas-to-dust ratio varies considerably
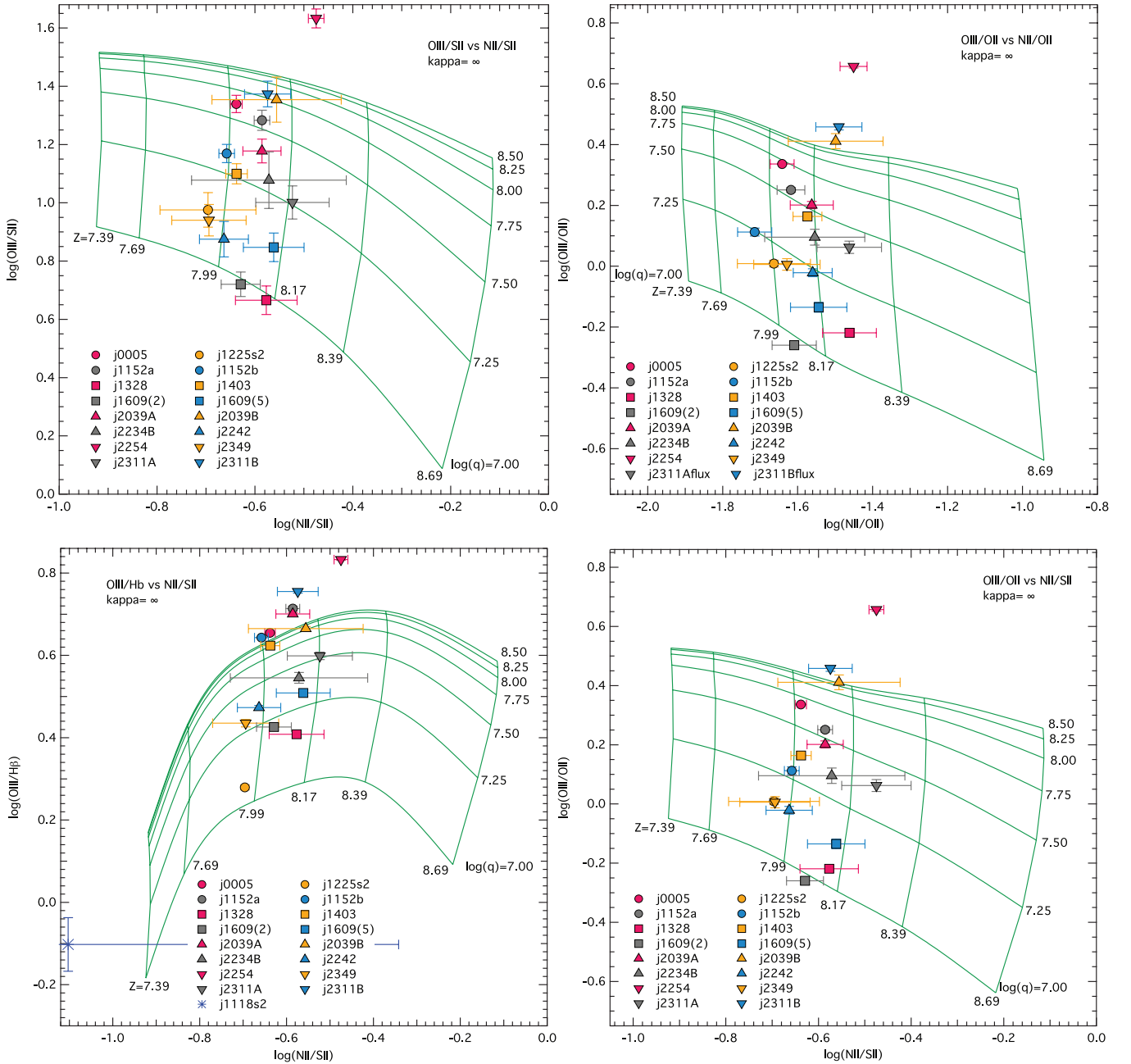
Figure 10. Observed flux ratios for SIGRID objects plotted on the O III/S II–N II/S II, O III/O II–N II/O II, O III/Hb–N II/S II and O III/O II–N II/S II grids.
(A color version of this figure is available in the online journal.)

between objects, depending on their individual star formation histories, particularly at the low end of the galaxy mass scale. This is a further complication for any attempt to estimate the total oxygen abundance in an H II region. López-Sánchez (2010) has shown a correlation between the reddening coefficient c(Hβ) and the gas-to-dust ratio in Wolf–Rayet galaxies, and it is likely that a similar relation holds for smaller dwarf galaxies. (We do not have the necessary FIR data to allow us to calculate the dust mass here.) In the meantime, the direct method oxygen abundance measurements provide a lower limit to the total oxygen.

4.4. log(N/O)

In this section we use the approach from our previous paper, Nicholls et al. (2014). One of the more important parameters in understanding galactic evolution is the nitrogen abundance, and

in particular, the ratio of nitrogen to oxygen. The observations reported here include relatively low noise measurements of both [N II] and [O II], allowing us to explore the values of log(N/O) for each H II region. To calculate the value of N/O from [N II] and [O II] line fluxes, we use empirical formulae from Izotov et al. (2006), Equations (3) and (6). (This approach was chosen because it accounts for the temperature dependencies of the [N II] and [O II] fluxes). These equations reduce to:

$$\log\left(\frac{N}{O}\right) = \log\left(\frac{N\,\text{II}\ 6584 + 6548}{O\,\text{II}\ 3726 + 3729}\right) + 0.273 - 0.726/T_{e4}$$

$$+ 0.007 \times T_{e4} - 0.02 \times \log\left(T_{e4}\right), \quad (11)$$

where T_{e4} is the [O III] electron temperature in units of 10,000 K. This equation differs only by a small constant offset (0.033) from

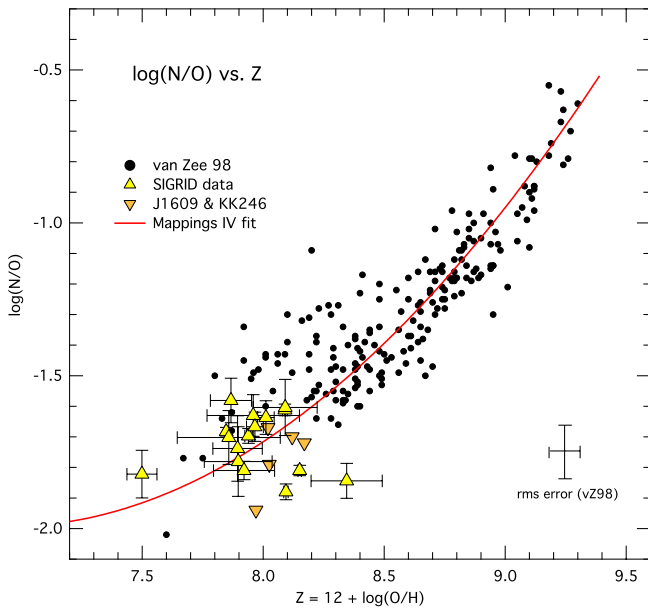**Figure 11.** Log(N/O) vs. oxygen abundance, Z. The triangles are for SIGRID objects, the black points are from van Zee et al. ([1998a]). The lower metallicity van Zee data are shown only for dwarf galaxies for which electron temperature metallicities are available.

(A color version of this figure is available in the online journal.)

Table 5
Calculated [S II] Line Ratios vs. Gas-phase Oxygen Abundance
($Z = 12 + \log(O/H)$) for $n_e = 10$ and 100 cm^{-3} and Ionization
Parameter $\log(q) = 7.5$

$12 + \log(O/H)$	$n_e = 10$	$n_e = 100$
7.39	1.439	1.394
7.69	1.439	1.393
7.99	1.439	1.391
8.17	1.44	1.389
8.39	1.441	1.384
8.69	1.445	1.373

Note. Calculated using Mappings IV photoionization code (Dopita et al. [2013]).

that quoted by Pagel et al. ([1992], Equation (9)), most probably due to the latter using older atomic data. We assume the same electron temperature for O II and N II (reasonable, as they both arise primarily from the outer parts of the H II region), and further, that $N^+/O^+ = N/O$, following Pilyugin et al. ([2010]) and others. The errors from these assumptions are likely to be of the same order as the measurement uncertainties. The results are shown in Table [6].

Using the abundance values listed in Table [6], we can plot $\log(N/O)$ versus oxygen abundance. Figure [11] shows the data from this work (yellow triangles), data from other SIGRID objects from Nicholls et al. ([2014]) (brown triangles) and data from van Zee et al. ([1998b]) (black circles). The SIGRID data are consistent with the van Zee results, without any obvious evidence of a floor. However, Berg et al. ([2012]) state that the nitrogen floor does not become apparent until the oxygen abundance falls below $Z = 7.7$, so the SIGRID data do not resolve the question of whether the floor exists. While the data for J1118−17s2 are not plotted because the value of the [N II] flux is not well defined, the best estimate values for this object ($\log(N/O) \lesssim 2.481$ and $Z \lesssim 7.2$) extend the trend considerably further in the same direction, off the graph, below and to the left. If correct, this suggests a very low level for any primary nitrogen, but further observations are necessary to confirm this The red curve is the fit to the van Zee data used in the Mappings model grids, from Dopita et al. ([2013], Figure 3), making allowance for the oxygen depletion into dust grains.

There is an increased scatter in the distribution with decreasing oxygen abundance (Z). Two possibilities may contribute to this. First, as there are populations of older stars in these galaxies (for example, KK246; Nicholls et al. [2014]), so intermediate mass asymptotic giant branch stars will contribute nitrogen to the ISM through hot-bottom burning processes. Second, the amounts contributed by such processes will depend on the (unknown) star formation histories of different galaxies. As the abundances derived using the strong-line diagnostics depend at least in part on the $\log(N\,II/O\,II)$ and $\log(N\,II/S\,II)$ ratios, the

results are sensitive to deviations in the nitrogen fit from the theoretical fit used in the Mappings models, which was derived from van Zee's ([1998a]) data (see Dopita et al. [2013]), so any error here affects the model outcomes.

Figure [11] shows that, at lower metallicities, the data exhibit increasing scatter and may even have started to fork into two branches. The upper region of the scatter may indicate nitrogen enrichment by Wolf–Rayet WN stars, as suggested by López-Sánchez & Esteban ([2010]). Smaller galaxies may divide into two classes, those with (or that have had) WN stars, and those without, depending on the stochastic nature of individual star formation events. Edmunds & Pagel ([1978]) have suggested the [N/O] ratio of H II regions in a galaxy arise from nitrogen that is significantly primary in origin, and are a measure of the early star formation history. While this may be correct for larger galaxies, at least in the case of the very isolated dwarf galaxy KK246, it is not the case, as the $\log(N/O)$ ratio is low but there is evidence of older stellar populations (Nicholls et al. [2014]). The presence or absence of WN stars in a dwarf galaxy's H II regions is a plausible explanation for this scatter or bifurcation. This would be consistent with the observations of the Blue Compact Dwarf galaxy, HS0837+4717 (Pustilnik et al. [2004]; Pérez-Montero et al. [2011]). The object appears to harbor over 100 Wolf–Rayet stars and has both a very low oxygen abundance and a high nitrogen abundance.

4.5. S II Line Ratios

The flux ratios of the two [S II] lines at 6716 and 6731 Å are good indicators of electron density (Section 5.6, Osterbrock & Ferland [2006]). Table [5] shows the variation of this ratio calculated for electron densities n_e of ~ 5 and ~ 50 cm^{-3}, for an ionization parameter $\log(q) = 7.5$, typical for H II regions. The trends in the [S II 6716]/[S II 6731] line ratio are due to two factors: (1) the relatively small dependence of the line ratio on $n_e\sqrt{T_e}$ resulting from the collisional excitation rates of the S II line upper states, and (2) the use of the isobaric setting in the Mappings photoionization modeling code, such that the density structure of the S II region is a function of the (varying) temperature within it, which depends on metallicity.

Table [6] shows the measured [S II] line ratios and electron densities, calculated using PyNeb (Luridiana et al. [2012]), for all objects except J1118−17s2, for which we have no electron temperature. Comparing the observed S II line flux ratios to Table [5], it is reasonable to conclude that the Mappings values show J0005−28, J1152−02A&B, J1403−27, J2039−63A, J2234−04B, J2254−26 have electron densities $n_e > 5$ cm^{-3}, while the remainder have $n_e < 5$ cm^{-3}. This is confirmed quantitatively using PyNeb to estimate the actual electron densities.
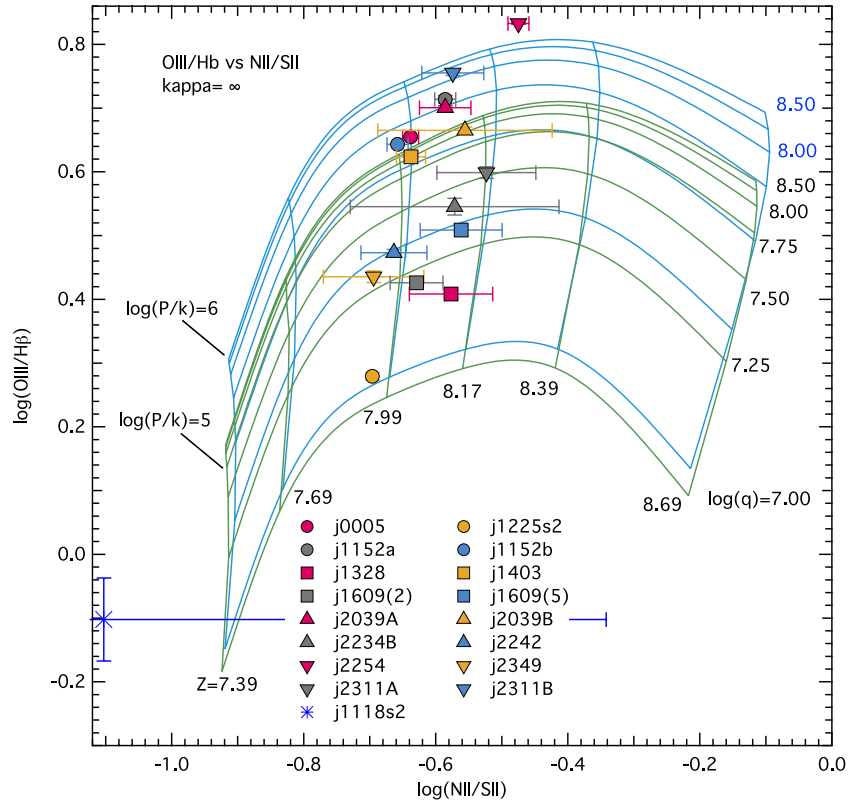
Figure 12. Comparison of diagnostic grids for the ratios $\log(\mathrm{O\,III}/H\beta)$ vs. $\log(\mathrm{N\,II}/\mathrm{O\,II})$ for electron densities $n_e \sim 5$ and ~ 50 cm^{-3} (isobaric case, $\log(P/k) = 5$ and 6, respectively, where P is the pressure and k is the Boltzmann constant.).

(A color version of this figure is available in the online journal.)

Table 6
Log(N/O), log(N II/O II), [S II] Line Ratios and Electron Densities

Object	$\log(\mathrm{N/O})$[a]	$\log(\mathrm{N\,II}/\mathrm{O\,II})$	S II Line Ratio[b]	n_e[c] (cm^{-3})
J0005$-$28	-1.683 ± 0.031	-1.641 ± 0.029	1.360 ± 0.092	57.5 ± 18.7
J1152$-$02A	-1.810 ± 0.033	-1.618 ± 0.033	1.385 ± 0.103	40.5 ± 36.9
J1152$-$02B	-1.880 ± 0.037	-1.715 ± 0.036	1.404 ± 0.099	24.0 ± 23.0
J1225$-$06s2	-1.822 ± 0.054	-1.663 ± 0.054	1.432 ± 0.158	—
J1328+02	-1.581 ± 0.052	-1.462 ± 0.045	1.540 ± 0.151	—
J1403$-$27	-1.697 ± 0.035	-1.574 ± 0.032	1.408 ± 0.106	$20.5\% \pm 100\%$
J1609$-$04b2	-1.844 ± 0.047	-1.609 ± 0.040	1.420 ± 0.121	$17.6\% \pm 100\%$
J1609$-$04b5	-1.630 ± 0.051	-1.544 ± 0.047	1.455 ± 0.141	—
J2039$-$63A	-1.667 ± 0.044	-1.562 ± 0.040	1.344 ± 0.114	$73.2\% \pm 100\%$
J2039$-$63B	-1.738 ± 0.067	-1.499 ± 0.067	1.501 ± 0.224	—
J2234$-$04B	-1.792 ± 0.069	-1.554 ± 0.069	1.389 ± 0.240	$35.5\% \pm 100\%$
J2242$-$06	-1.813 ± 0.038	-1.560 ± 0.038	1.497 ± 0.176	—
J2254$-$26	-1.612 ± 0.033	-1.451 ± 0.032	1.317 ± 0.095	96.8 ± 34.0
J2311$-$42A	-1.605 ± 0.060	-1.463 ± 0.052	1.473 ± 0.160	—
J2311$-$42B	-1.637 ± 0.046	-1.490 ± 0.041	1.456 ± 0.132	—
J2349$-$22	-1.702 ± 0.059	-1.628 ± 0.051	1.457 ± 0.150	—

Notes.

[a] lLog(N/O) calculated from N II/O II flux ratios using Equation (11) and electron temperatures from Table 4.

[b] n_e uncertainties calculated using the line ratio uncertainties, except where these are large, where they exceed the value of n_e, and are quoted as 100%.

[c] "—" indicates electron densities $\lesssim 5$ cm^{-3}.

Figure 12 shows the diagnostic grids for O III/Hβ versus N II/S II at the two electron densities—the blue (upper) grid is for $n_e \sim 50$ cm^{-3}, the green (lower) is for ~ 5 cm^{-3}. It is clear that all but J2254$-$26 can be accommodated even on the higher electron density grid. The abundances for each object are very similar on both grids, but the estimated ionization parameter $\log(q)$ changes. Similar results apply for the other diagnostic

grids. It is interesting to note that J2254$-$26 has the highest calculated electron density of the observed objects.

4.6. T_e: Oxygen Gas-phase Abundance

Figure 13 shows electron temperature, plotted versus gas-phase oxygen abundance, Z, from Table 4. Z ($=12+\log(\mathrm{O/H})$)
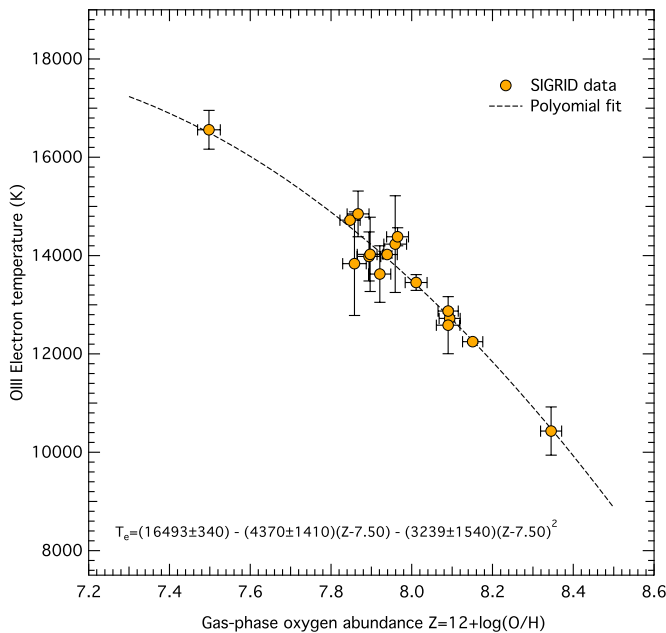
Figure 13. Electron temperature, T_e, vs. gas-phase oxygen abundance for the SIGRID objects, calculated using Equations (2) and (5).

(A color version of this figure is available in the online journal.)

is derived using the formulae in Equations (2) and (5). The quadratic fit to the data with 66% confidence errors is:

$$T_e = -(0.3239 \pm 0.1540)(Z - 7.50)^2 - (0.4370 \pm 0.1410)$$
$$\times (Z - 7.50) + (1.6493 \pm 0.0340)) \times 10^4. \quad (12)$$

While Figure 13 may be used to calculate the total gas-phase oxygen abundance from the [O III] electron temperature, it applies only to the data presented here, and we will provide a substantially more accurate fit to the model-derived curve in Paper II.

5. DISCUSSION

5.1. Mass–Metallicity

Mass (or luminosity) versus metallicity behavior is one of the important evolutionary diagnostics for galaxies. It has been extensively mapped for larger galaxies (e.g., Tremonti et al. 2004), but it is less well known for dwarf galaxies. It has been studied by several authors (Lee et al. 2006; Pustilnik et al. 2011; Berg et al. 2012; Andrews & Martini 2013). Exploring it was one of the initial motivations for the SIGRID sample (Nicholls et al. 2011). Figure 14 shows the gas-phase oxygen abundance versus neutral hydrogen mass (left panel, data from Meurer et al. (2006) and Table 1) and gas-phase oxygen abundance versus absolute *B*-band magnitude (right panel).

There is no clear trend in the first graph, suggesting the neutral hydrogen mass is not strongly correlated with metallicity, at least in this sample. In the right panel, we compare the SIGRID data against data from the Pustilnik et al. (2011) survey of galaxies in the Lynx-Cancer void. The SIGRID data are consistent with the Pustilnik et al. data, and both samples are selected for isolation. The four blue points in the right panel are objects from Pustilnik et al., but which meet the more stringent selection criteria for the SIGRID sample, for luminosity, galaxy type and isolation (distance from nearest neighbor). The trend line is from Lee et al. (2003) for field dI galaxies, but which were not otherwise

selected for isolation. Both the Pustilnik and SIGRID data tend to fall below the line, indicating that more isolated objects have slightly lower metallicities than similar objects in more congested regions, as suggested by Pustilnik et al. (2011).

There is insufficient data in our observations to confirm the increasing spread of metallicity values at low mass, as implied by Tremonti et al. (2004, Figure 6). However, the log(N/O) data (Figure 11) are consistent with such a spread.

5.2. Comparison of Metallicity Methods

In this work, we have calculated the gas-phase oxygen abundance using the electron temperature direct method routine developed here, and the diagnostic grids. Table 4 compares the electron temperature abundances using the methods described here with those using the iterative method from Izotov et al. (2006), with the same input temperatures; and the most reliable values from the diagnostic grids, those using the log(N II/S II) and log(N II/O II)diagnostics. The values derived using the two T_e methods are similar, suggesting that the method developed here is reliable. See also a discussion of this in the forthcoming Paper II.

It is interesting to note that the diagnostic grid abundances, with two notable exceptions, are consistently a little higher than the direct method values, consistent with the findings of López-Sánchez et al. (2012). The average value of the difference δZ is 0.104 ± 0.171. The complete explanation of this difference is unclear, but in part it can be explained by the nature of the diagnostic grids derived from the Mappings photoionization modeling code. In the grids, we have assumed a dust depletion of 1.0 solar (Dopita et al. 2013), to account for the elements locked up in dust grains. This leads to an overestimate of 0.07 dex in the abundance values derived from the diagnostic grids, compared to the gas-phase-only oxygen abundances from the direct method, explaining about half of the discrepancy.

It is useful to examine two of the "outliers" in Table 4, where the diagnostic grid oxygen abundances differ substantially from the electron temperature oxygen abundances. J1225−06s2 has a very low oxygen abundance, ∼7.45, from the direct method, and ∼7.9 from the grids. This could be explained if there is more N II than implied by the Mappings models parameters, although this is not obvious from Table 6. There may also be increased nitrogen due to enrichment by WN stars, as in the case of HS 0837+4717 (Pustilnik et al. 2004; Pérez-Montero et al. 2011). The oxygen abundance discrepancy for J1609−04(2) is very likely a result of uncertainty in the flux of the [O III] 4363 Å auroral line, which is weak in this object.

The diagnostic grids themselves (Table 3) are somewhat discrepant in the values yielded for oxygen abundances. In particular, two trends are clear. First, diagnostics involving log(N II/S II) are particularly consistent, and the closest to the oxygen abundances derived using the direct method. Diagnostics involving [O II] fluxes are nearly as consistent. This concordance and consistency lead us to believe that these diagnostics are the most reliable, and we have used the means of the log(N II/S II) and log(N II/O II)diagnostics in Table 4. Second, diagnostics involving log(N II/Hα) give somewhat higher oxygen abundances than both the other diagnostics and the direct method values. The source of these discrepancies is unclear, but may be related to the abundance fit for nitrogen used in Mappings. They do not materially affect the results reported here, provided we rely on the log(N II/S II) and log(N II/O II) diagnostics and direct method oxygen abundances.
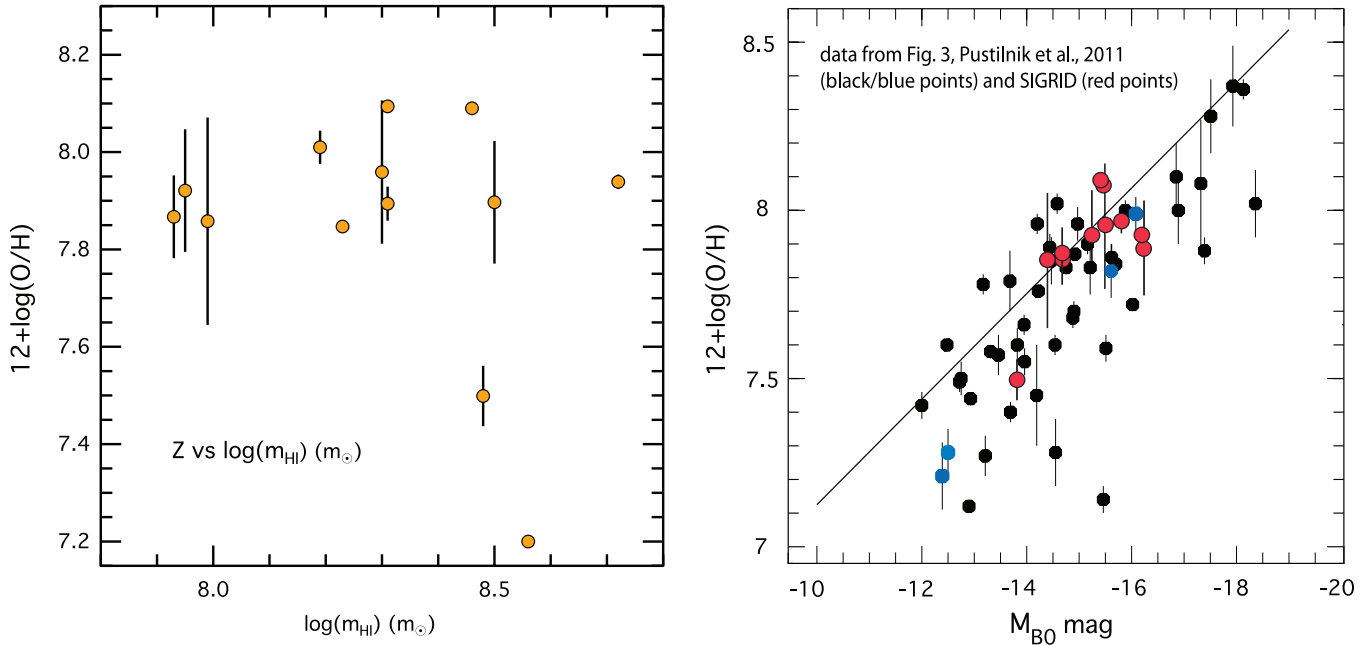
Figure 14. Left panel: oxygen abundance vs. neutral hydrogen mass (from Table 1). Right panel: oxygen abundance vs. absolute *B*-band magnitude, comparing data from Figure 3 from Pustilnik et al. (2011) with SIGRID data. Eleven SIGRID objects have measured *B*-band magnitudes. The four blue points are those from the Pustilnik sample which meet the luminosity, galaxy type, and isolation selection criteria for SIGRID. The straight line fit is for field dI galaxies from Lee et al. (2003). The *B*-band magnitudes for the SIGRID sample have been taken from the NASA Extragalactic Database (NED).

(A color version of this figure is available in the online journal.)

5.3. Further Analysis and Investigations

In the second paper examining these observations, we will explore the effect of three-dimensional diagnostic charts. These use three independent diagnostic ratios plotted and explored in three dimensions, whose purpose is to investigate whether the observations lie on a diagnostic plane, along the lines of F. P. A. Vogt at al. (2014, in preparation). We will examine the effects of using diagnostic grids calculated using higher electron densities. We will investigate the effects of optically thin H II regions, and show that they can have considerable effects on the diagnostics, and that there is evidence of optical thinness in some of the observed objects. We will re-examine the electron temperature versus oxygen abundance plots, for both these observations and for 124 SDSS objects from Izotov et al. (2006). Using the Mappings photoionization modeling code, we will demonstrate that with reasonable assumptions about the star clusters exciting H II regions, there is an effective upper limit to the temperature that can be reached, even in optically thin regions. The implications appear to be that some of the high temperatures reported in low metallicity H II regions may be somewhat in error. We will demonstrate the effect of taking into account the additional contribution to total oxygen abundance of the oxygen in dust grains. We will also suggest that the apparent spread in metallicities at the low end of the mass-metallicity relation are due to stochastic effects in stellar mass distributions in the small star clusters exciting H II regions in small irregular galaxies.

6. CONCLUSIONS

In this paper we have presented the results of observations of 17 H II regions in thirteen small isolated dwarf irregular galaxies, most from the SIGRID sample, all but one exhibiting the [O III] auroral line. All have measured oxygen abundances <8.2 (<0.3 $Z_\odot$), one has an apparent abundance of 7.44 and another very low metallicity object with $Z \sim 7.2$. We have derived

a method for calculating total gas-phase oxygen abundances using only the optical spectra between 3700 and 7000 Å. This method gives very similar results to previous empirical fit methods. From an analysis of abundances and ionization coefficients using the diagnostic grids developed by Dopita et al. (2013), we find the direct method oxygen abundances are consistently within 0.07 dex of the strong-line diagnostic results, making allowance for the oxygen locked up in dust grains. From the line ratio of the two red [S II] lines we find that the electron densities occurring in the objects observed are between ∼5 and 100 cm^{-3}. The nitrogen abundance, as expressed in log(N/O), continues the trend evident in van Zee et al. (1998b), but from this sample we find no clear evidence for a nitrogen floor. There is increased scatter at lower oxygen abundances, and some evidence for a bifurcation in the trend, possibly due to the presence of WN stars in some of the H II regions. The slope of the luminosity–metallicity relation for these observations is very close to that for void galaxies in Pustilnik et al. (2011). The spectra from an apparently very low metallicity galaxy, J1118−17s2, show no nitrogen lines: we intend to undertake follow up observations on this galaxy to estimate the metallicity more accurately.

APPENDIX

EMISSION LINE FLUX ERROR ESTIMATION

This Appendix describes the methods used to estimate emission line flux uncertainties for spectra extracted from WiFeS

data cubes of objects in the SIGRID sample. The data reduction process is described in detail in Childress et al. (2013), and in this paper in Section 2.3. Briefly, the steps where noise is involved or systematic errors are incurred are bias subtraction, flat fielding, cosmic ray removal, sky-line subtraction using nod-and-shuffle, and standard flux star calibration. The principle sources of uncertainty are the CCD detector and amplifier readout noise, and the amplification of this noise through the data reduction chain; the effects of cosmic rays and sky lines, and their removal (partial or complete); the calibration of the emission line fluxes using standard star flux data; the de-reddening process; and the measurement of the line fluxes from the flux-calibrated spectra.

As the IFU data frame is convolved into a data cube in the pipeline, the process of error calculation is more complex than for single slit or echelle spectroscopy. For the spectral noise uncertainties, there are two approaches we could take. One is to estimate the errors accumulating from each step, such as described for echelle spectroscopy by Skillman et al. (1994). The other approach, used here, is to measure the statistical noise from spectra extracted from the reduced data cube, and to estimate the systematic errors arising from the de-reddening and flux calibration, which are independent of the statistical noise. Unlike single slit spectra, with IFU data cubes, we are able to select the entire area of the H II region from which to extract the spectrum, and exclude the majority of the galaxy stellar background, resulting in better signal-to-noise. Note that the statistical noise varies with the size of the sampled spaxel area, due to averaging. For the objects in this study, sampling using a 6 arcsec diameter circular spatial area maximizes the amount of flux from the H II region and minimises both the statistical noise, though averaging, and the stellar continuum from the area outside the H II region.

In every case, the galaxies were so faint that the stellar extent was at best barely detectable. However, images from the DSS survey and from the SINGG data (as illustrated in Nicholls et al. 2011) suggest the individual galaxies are less than or approximately equal to the FOV of the WiFeS spectrograph, 25×38 arcsec. The benefit of the IFU is that the sample was centered on the H II region, and excluded virtually all areas of the galaxies without H II emission.

Line fluxes and noise were measured from the extracted spectra using IRAF/splot. The standard splot "k–k" method was used to fit a Gaussian to each emission line, to measure the equivalent width (where possible), the Gaussian full width at half-maximum, and the integrated flux. Noise was measured on both sides of the emission line using the splot "m-m" method. These results were checked using the deblend "d–d" method, but using a single line, which automatically generates values of the same parameters. Particular care was taken to account for any stellar absorption features underlying the Balmer emission lines, although in all cases, this was minor or absent, due to low stellar continuum. In fact, the stellar continuum was extremely faint, with the exception of the object J0005−28 (see Figure 8, displayed on a log–intensity scale). Test sample sizes showed that all the detectable Hα and [O III] in each H II region lay within the sample aperture. The observed fluxes mostly peak at or less than a radius of 2.5 arcsec, except where there are closely adjacent H II regions (e.g., J1609−04). For these, limiting the sample size to 6 arcsec diameter avoided sampling a different H II region. Ideally, single spaxel-based analysis would be preferable to multi-spaxel sampling, but these objects are so faint that the resultant noise is prohibitive.
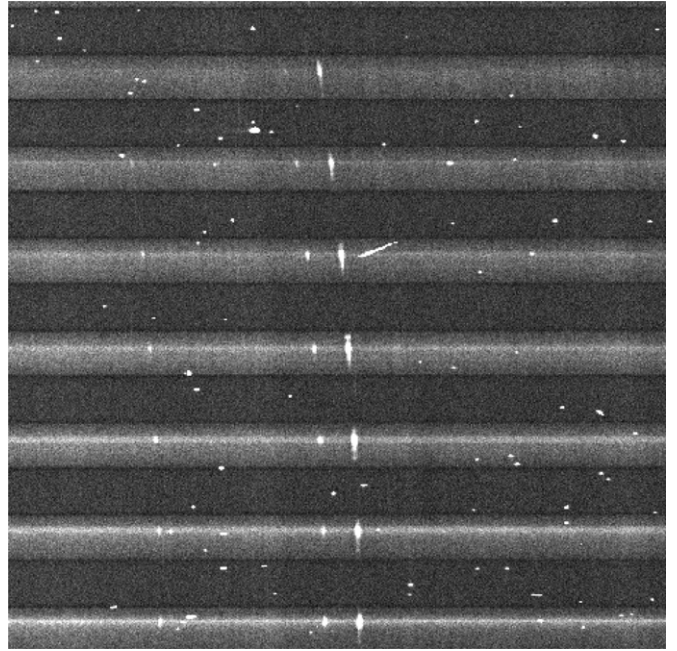

Figure 15. Section of a single WiFeS IFU raw data frame for J0005−28 with cosmic ray artefacts, centered on the Hγ line, showing sections of seven slitlets. Each frame was inspected to check for cosmic ray contamination of key lines. Note that, due to the optical paths in the WiFeS IFU blue camera, the right side of the image corresponds to shorter wavelengths.

Detector noise is added to the data frame during bias subtraction and flat fielding, as the bias and flat field frames used also incur readout noise. The sky subtraction process using the nod and shuffle process or the sky frame method adds additional noise during the subtraction process. Nod-and-shuffle sky subtraction was used for all H II region observations, with sub-exposure times chose to be shorter than the shortest observed fluctuation in the OH airglow lines (Frey et al. 2000). The removal of the critical OH lines is effectively complete in all observations. The [O I] airglow lines are at wavelengths that did not interfere with any of the observed H II region spectral lines.

Cosmic ray removal is reasonably efficient, using the Laplacian kernel technique described by van Dokkum (2001). The process is not perfect, but virtually all the remaining cosmic ray artefacts are removed using the `imcombine` process. In isolated cases, separate cosmic rays occur on all object data frames at the same location, and this can lead to erroneous results, but this can be detected by the labor intensive process of inspecting all the lines on all the IFU slitlets (25) on all the data frames (usually 3). Figure 15 shows part of a raw WiFeS blue data frame including segments of 7 slitlets (of a total 25), centered on the Hγ and [O III] λ 4363 auroral line, for the galaxy J0005−28. The auroral line is very prominent in this frame, to the left of the Hγ line.

In addition to the intrinsic statistical noise amplified through the data reduction pipeline, when measuring the emission line fluxes, it is necessary to take into account any broad absorption lines in the stellar continuum, on which the nebular spectra are superimposed. There are three approaches here. The first is to correct for an assumed 2 Å equivalent width (EW) absorption in each line, as described in Skillman et al. (1994). The second is to use an automated method such as the LZIFU IDL program developed by several workers at the University of Hawaii, which fits model stellar continua to observed spectra and then

calculates the emission line fluxes (a paper on this application is planned). The third approach, which we use here, works better when the stellar continuum is weak, as with the objects reported here. It involves manual fitting of Gaussian profiles to the emission lines using standard IRAF/splot methods. The technique described by Berg et al. (2013) is very similar in detail to the method used here.

The errors arising from the de-reddening process are due to uncertainties in the nature and amount of dust between the nebular emission and the observer. In the case of the SIGRID objects considered here, all are further than $10°$ from the galactic equator, to avoid significant reddening by Milky Way dust. We calculated the de-reddening using two independent methods and used the differences between the results as an estimate of the de-reddening errors. We used the dust reddening formulae from Cardelli et al. (1989) with $A_V = 3.1$, adjusting the de-reddening to set the resultant Balmer Hα/Hβ flux ratios to the Storey & Hummer (1995) Case B Balmer ratios for the calculated [O III] electron temperature. We used the ratios of Hγ and Hδ to Hβ as confirmation. To confirm these results, we employed the dust models from Fischera & Dopita (2005), using a relative extinction curve with $R_V^A = 4.3$, where $R_V^A = A_V/(E_{B-V})$ and A_V is the V-band extinction. This is discussed in more detail in Vogt et al. (2013, Appendix 1). We used an initial Balmer decrement ratio of 2.82 for Hα/Hβ, corresponding to an electron temperature of 12,500 K, adjusted the electron temperature using the direct method derived from the [O III] line ratios, then adjusted the apparent Balmer ratios by varying the value of A_V for the best fit to the Hγ/Hβ ratio, using the ratio Hδ/Hβ as a check, again fitting to the Storey and Hummer Case B Balmer ratios.

The de-reddened flux values reported in Table 2 are those using the Cardelli method. In all cases, the two approaches gave similar results: The average difference between the two methods for the important diagnostic lines varies between 0.1% and 0.7%. As a consequence, we have adopted a figure of 1% for the de-reddening error. In only one case, J2234−04, object A, did the de-reddening fail to provide a plausible result, and this has been excluded from the results reported here. It appears likely that two or more incompletely removed sets of cosmic ray artefacts were the cause of the problem, in this particular case.

Flux calibration errors depend on how well one can fit flux-calibrated vales to the standard stars. The standard stars used were taken from Bessell (1999), using Bessell's recalibration of Hamuy's Southern Spectrophotometric Standards Hamuy et al. (1992). Calibrating to these standards is likely to be more accurate than the older Oke standards (Oke 1990), but we have retained an estimated 2% error for calibrating the flux values, as per Berg et al. (2013).

We have recently corrected a problem with the measured [O II] line fluxes. The source of the problem is a sharp absorption edge at 3850 Å, due to the adhesive used in the beam splitter, and the lack of any significant output below about 3900 Å from the lamps used for flat exposures to identify and correct this problem. The lamps are now being replaced, and future measurements using WiFeS will no longer require this compensation. The problem was understood in the testing phase of the construction of WiFeS, and was identified in the observations from poor matches to the diagnostic grids that involve [O II] in the ratios. To compensate requires boosting the [O II] flux by a factor of times 1.5. It affects only the [O II] $\lambda\lambda$ 3726,9 lines. It does not make a substantial difference to the calculated oxygen abundances or other results.

REFERENCES

Andrews, B. H., & Martini, P. 2013, ApJ, 765, 140
Berg, D. A., Skillman, E. D., Garnett, D. R., et al. 2013, ApJ, 775, 128
Berg, D. A., Skillman, E. D., Marble, A. R., et al. 2012, ApJ, 754, 98
Bessell, M. S. 1999, PASP, 111, 1426
Cardelli, J. A., Clayton, G. C., & Mathis, J. S. 1989, ApJ, 345, 245
Childress, M. J., Vogt, F. P. A., Nielsen, J., & Sharp, R. G. 2013, Ap&SS, 349, 617
Contini, T., Treyer, M. A., Sullivan, M., & Ellis, R. S. 2002, MNRAS, 330, 75
Dopita, M. A., Hart, J., McGregor, P., et al. 2007, Ap&SS, 310, 255
Dopita, M. A., Rhee, J., Farage, C., et al. 2010, Ap&SS, 327, 245
Dopita, M. A., & Sutherland, R. S. 2003, Astrophysics of the Diffuse Universe (Berlin: Springer)
Dopita, M. A., Sutherland, R. S., Nicholls, D. C., Kewley, L. J., & Vogt, F. P. A. 2013, ApJS, 208, 10
Edmunds, M. G., & Pagel, B. E. J. 1978, MNRAS, 185, 77P
Fischera, J., & Dopita, M. 2005, ApJ, 619, 340
Frey, H. U., Mende, S. B., Arens, J. F., McCullough, P. R., & Swenson, G. R. 2000, GeoRL, 27, 41
Garnett, D. R. 1992, AJ, 103, 1330
Hamuy, M., Walker, A. R., Suntzeff, N. B., et al. 1992, PASP, 104, 533
Izotov, Y. I., Stasińska, G., Meynet, G., Guseva, N. G., & Thuan, T. X. 2006, A&A, 448, 955
Kewley, L. J., & Dopita, M. A. 2002, ApJS, 142, 35
Kewley, L. J., & Ellison, S. L. 2008, ApJ, 681, 1183
Lee, H., McCall, M. L., Kingsburgh, R. L., Ross, R., & Stevenson, C. C. 2003, AJ, 125, 146
Lee, H., Skillman, E. D., Cannon, J. M., et al. 2006, ApJ, 647, 970
López-Sánchez, Á. R. 2010, A&A, 521, 63
López-Sánchez, Á. R., Dopita, M. A., Kewley, L. J., et al. 2012, MNRAS, 426, 2630
López-Sánchez, Á. R., & Esteban, C. 2010, A&A, 517, A85
Luridiana, V., Morisset, C., & Shaw, R. A. 2012, in IAU Symp. 283, Planetary Nebulae: An Eye to the Future, ed. A. Manchado, L. Stanghellini, & D. Schoenberner (Cambridge: Cambridge Univ. Press), 422
McGaugh, S. S. 1994, ApJ, 426, 135
Meurer, G. R., Hanish, D. J., Ferguson, H. C., et al. 2006, ApJS, 165, 307
Meyer, M. J., Zwaan, M. A., Webster, R. L., et al. 2004, MNRAS, 350, 1195
Nicholls, D. C., Dopita, M. A., Jerjen, H., & Meurer, G. R. 2011, AJ, 142, 83
Nicholls, D. C., Dopita, M. A., & Sutherland, R. S. 2012, ApJ, 752, 148
Nicholls, D. C., Dopita, M. A., Sutherland, R. S., Kewley, L. J., & Palay, E. 2013, ApJS, 207, 21
Nicholls, D. C., Jerjen, H., Dopita, M. A., & Basurah, H. 2014, ApJ, 780, 88
Oke, J. B. 1990, AJ, 99, 1621
Osterbrock, D. E., & Ferland, G. J. 2006, Astrophysics of Gaseous Nebulae and Active Galactic Nuclei (2nd ed.; Mill Valley, CA: Univ. Science Books)
Pagel, B. E. J., Simonson, E. A., Terlevich, R. J., & Edmunds, M. G. 1992, MNRAS, 255, 325
Palay, E., Nahar, S. N., Pradhan, A. K., & Eissner, W. 2012, MNRAS, 423, L35
Pérez-Montero, E., & Contini, T. 2009, MNRAS, 398, 949
Pérez-Montero, E., Vílchez, J. M., Cedrés, B., et al. 2011, A&A, 532, A141
Pilyugin, L. S., & Thuan, T. X. 2005, ApJ, 631, 231
Pilyugin, L. S., Vílchez, J. M., & Thuan, T. X. 2010, ApJ, 720, 1738
Pustilnik, S., Kniazev, A., Pramsky, A., et al. 2004, A&A, 419, 469
Pustilnik, S. A., Tepliakova, A. L., & Kniazev, A. Y. 2011, AstBu, 66, 255
Rémy-Ruyer, A., Madden, S. C., Galliano, F., et al. 2014, A&A, 536, A31
Skillman, E. D., Televich, R. J., Kennicutt, R. C., Jr., Garnett, D. R., & Terlevich, E. 1994, ApJ, 431, 172
Storey, P. J., & Hummer, D. G. 1995, MNRAS, 272, 41
Sung, E., Chun, M., Freeman, K. C., & Chaboyer, B. 2002, in ASP Conf. Ser. 273, The Dynamics, Structure & History of Galaxies: A Workshop in Honour of Professor Ken Freeman, ed. G. S. Da Costa & H. Jerjen (San Francisco, CA: ASP), 341
Sweet, S. M., Drinkwater, M. J., Meurer, G., et al. 2014, ApJ, 782, 35
Tayal, S. S. 2007, ApJS, 171, 331
Tremonti, C. A., Heckman, T. M., Kauffmann, G., et al. 2004, ApJ, 613, 898
van Dokkum, P. G. 2001, PASP, 113, 1420
van Zee, L., & Haynes, M. P. 2006, ApJ, 636, 214
van Zee, L., Salzer, J. J., & Haynes, M. P. 1998a, ApJL, 497, L1
van Zee, L., Salzer, J. J., Haynes, M. P., O'Donoghue, A. A., & Balonek, T. J. 1998b, AJ, 116, 2805
Vila Costas, M. B., & Edmunds, M. G. 1993, MNRAS, 265, 199
Vogt, F. P. A., Dopita, M. A., & Kewley, L. J. 2013, ApJ, 768, 151